



UPPSALA
UNIVERSITET

*Digital Comprehensive Summaries of Uppsala Dissertations
from the Faculty of Science and Technology 1996*

Aeroacoustic Prediction for Vertical Axis Wind Turbines

AYA AIHARA



ACTA
UNIVERSITATIS
UPSALIENSIS
UPPSALA
2021

ISSN 1651-6214
ISBN 978-91-513-1090-9
urn:nbn:se:uu:diva-426038

Dissertation presented at Uppsala University to be publicly examined in Polhemsalen, Ångströmlaboratoriet, Lägerhyddsvägen 1, Uppsala, Friday, 5 February 2021 at 13:15 for the degree of Doctor of Philosophy. The examination will be conducted in English. Faculty examiner: Professor Mats Åbom (KTH Royal Institute of Technology, The Marcus Wallenberg Laboratory).

Abstract

Aihara, A. 2021. Aeroacoustic Prediction for Vertical Axis Wind Turbines. *Digital Comprehensive Summaries of Uppsala Dissertations from the Faculty of Science and Technology* 1996. 90 pp. Uppsala: Acta Universitatis Upsaliensis. ISBN 978-91-513-1090-9.

This thesis investigates the aerodynamic and aeroacoustic prediction of vertical axis wind turbines, using computational fluid dynamics simulations. Noise pollution from wind turbines is one of the disadvantages of wind energy, calling for strategies to reduce noise levels. Yet for vertical axis wind turbines in particular, there is insufficient knowledge of how to identify sound sources and mitigate the sound level. The aim of this study is to predict aerodynamic noise, using large eddy simulation and acoustic analogy, so as to better understand the mechanism of sound generation for vertical axis wind turbines. First, the prediction method is validated for a static single blade in stall. This model is able to capture the dominant frequency, but it does not well reproduce the broadband characteristics. Next, the aerodynamic behavior of the 12 kW H-rotor vertical axis wind turbine is studied, whereby the focus is on the importance of properly modeling the strut influence for an accurate prediction of the blade forces. To achieve this, the flow field is solved for three different tip speed ratios. The results show that the struts significantly affect on the force distribution along the blade. The reduction of the blade force is observed to occur not only at the attachment points of the struts, but also over a large area of the blade section in the downwind side where the blade interacts with the wake created in the upwind. Finally, the noise radiated from the vertical axis wind turbine operating at high tip speed ratio is predicted. Measurements are conducted to validate the prediction, with the experimental data representing the broadband noise characteristics dominant at around 800 Hz. The prediction reproduces the sound pressure level observed at a radial distance of 1.4 rotor diameter, with a few decibels difference. However, these discrepancies become more pronounced at double distance, which can be considered to arise due to the effect of the ground reflection being ignored. The simulation furthermore indicates, that the main sound sources are emitted when the blade rotates in the downwind. It is suggested that future work should properly consider the atmospheric turbulence for more accurate predictions.

Keywords: fluid, acoustics, noise, sound, wind energy, vertical axis wind turbine, aerodynamics, airfoil, simulations, CFD, LES

Aya Aihara, Department of Electrical Engineering, Electricity, Box 534, Uppsala University, SE-751 21 Uppsala, Sweden.

© Aya Aihara 2021

ISSN 1651-6214

ISBN 978-91-513-1090-9

urn:nbn:se:uu:diva-426038 (<http://urn.kb.se/resolve?urn=urn:nbn:se:uu:diva-426038>)

To my parents

List of papers

This thesis is based on the following papers, which are referred to in the text by their Roman numerals.

- I **A. Aihara**, A. Goude, and H. Bernhoff. LES prediction for acoustic noise of airfoil at high angle of attack. In *Proceedings of AIAA Scitech 2020 Forum*, Florida, USA, January, 2020.
- II **A. Aihara**, A. Goude, and H. Bernhoff. Numerical prediction of noise generated from airfoil in stall using LES and acoustic analogy. *Submitted to Noise & Vibration Worldwide*, October, 2020.
- III **A. Aihara**, V. Mendoza, A. Goude, and H. Bernhoff. A numerical study of strut influence on blade forces of vertical axis wind turbine using computational fluid dynamics simulation. *Submitted to Wind Energy*, June, 2020.
- IV **A. Aihara**, V. Mendoza, A. Goude, and H. Bernhoff. Comparison of three-dimensional numerical methods for modeling of strut effect on aerodynamic forces of a vertical axis wind turbine. *Submitted to Wind Energy*, October, 2020.
- V **A. Aihara**, K. Bolin, A. Goude, and H. Bernhoff. Aeroacoustic noise prediction of a vertical axis wind turbine using Large Eddy Simulation. *Submitted to International Journal of Aeroacoustics*, December, 2020.

Reprints were made with permission from the publishers.

Contents

1	Introduction	13
1.1	Perspectives of wind energy	13
1.2	Wind turbine technologies	14
1.3	Wind turbine noise	15
1.3.1	Mechanical noise	16
1.3.2	Aerodynamic noise	16
1.4	Previous studies for wind turbine noise	17
1.5	Contribution of this thesis	19
1.6	Outline of the thesis	19
2	Theory	20
2.1	Acoustic analogy	20
2.1.1	Curle's analogy	20
2.1.2	Ffowcs Williams and Hawkings analogy	21
2.2	Spanwise correction	23
2.3	Basic aerodynamics of wind turbines	25
3	Description of the 12 kW vertical axis wind turbine at Marsta	28
4	Validation of noise prediction	31
4.1	Study case	31
4.2	Numerical method	32
4.3	Results and discussion	34
4.3.1	Flow characteristics	34
4.3.2	Verification for spanwise correction	36
4.3.3	Influence of boundary condition	39
4.3.4	Comparison with measurement	39
5	Aerodynamic studies for vertical axis wind turbine	41
5.1	Numerical method	41
5.2	Validation of numerical method	44
5.3	Results and discussion	45
5.3.1	Comparison with different numerical methods	46
5.3.2	Case study for high tip speed ratio	54
6	Aeroacoustic studies for vertical axis wind turbine	58
6.1	Numerical method	58
6.2	Acoustic measurement	58

6.3	Results and discussion	61
7	Conclusions	74
8	Future work	76
9	Summary of papers	77
10	Acknowledgements	80
11	Svensk sammanfattning	81
12	研究概要	83
	References	85

Nomenclature

Symbol	SI-unit	Description
C_n	-	Normal force coefficient
C_t	-	Tangential force coefficient
c	m	Chord length
c_0	m/s	Speed of the sound
D	m	Rotor diameter
F_n	N	Normal force
F_t	N	Tangential force
f	Hz	Frequency
H	m	Blade length
K	-	Kármán constant
L	m	Total span length
L_c	m	Spanwise coherence length
L_s	m	Simulated span length
N_B	-	Number of blades
p	Pa	Pressure
p_0	Pa	Pressure in a reference fluid at rest
p_{ref}	Pa	Reference sound pressure (thresholds of human hearing, 20 μ Pa)
p'	Pa	Sound pressure
p'_L	Pa	Sound pressure of loading noise
p'_T	Pa	Sound pressure of thickness noise
p'_{all}	Pa	Sound pressure generated from the total span length L
p'_s	Pa	Sound pressure generated from the simulated span length L_s
\dot{p}	Pa/s	Time derivative of pressure
Q	1/s	Second invariants of the velocity gradient tensor
R	m	Rotor radius
SPL_{all}	-	Sound pressure level generated from the total span length L
SPL_{corr}	-	Sound pressure level for correction
SPL_s	-	Sound pressure level generated from the simulated span length L_s
U	m/s	Flow velocity
U_0	m/s	Freestream velocity
U_∞	m/s	Freestream velocity at hub height
U_{rel}	m/s	Relative flow velocity
z_0	m	Roughness length

Symbol	SI-unit	Description
α	-	Angle of attack
α_*	-	Effective aerodynamic angle of attack
α_t	-	Angle of attack referenced to streamwise axis
γ	-	Spanwise coherence function
Δz	m	Spanwise distance
θ	-	Azimuth angle
λ	-	Tip speed ratio
ρ	kg/m ³	Density of the air
ρ_0	kg/m ³	Density of the air in a reference fluid at rest
σ	-	Solidity
τ	s	Retarded time
τ_{ij}	Pa	Viscous stress
φ	-	Angle of relative wind
φ_0	-	Geometric angle of relative wind
ω	rad/s	Rotational speed

Abbreviations

Abbreviations	Description
ALM	Actuator line model
CFD	Computational fluid dynamics
HAWT	Horizontal axis wind turbine
LES	Large eddy simulation
RANS	Reynolds-averaged Navier–Stokes
SGS	Subgrid scale
SPL	Sound pressure level
VAWT	Vertical axis wind turbine

1. Introduction

This thesis is based on the aerodynamics and aeroacoustics of wind turbines. The main focus here is to predict the sound emission of vertical axis wind turbines. Wind turbines give rise to complex aerodynamic phenomena which, in turn, generate various aeroacoustic noise sources. To date, several studies have been reported on the mechanism of sound generation. The present chapter provides a general background to wind turbine noise, and briefly outlines current experimental and numerical research in this field.

1.1 Perspectives of wind energy

Wind power is one of the major renewable resources and, owing to considerable advancements in technology, has been the fastest growing energy source over the last decades. According to statistics published by the WWEA [1], 60 GW of global wind capacity were installed in 2019 alone, with the overall capacity reaching 651 GW by the end of that year. All wind turbines installed by the end of 2018 can cover more than 6% of the global electricity demand. WindEurope [2] states that Europe installed 15 GW of new wind power capacity in 2019, and now has 205 GW of wind energy capacity. Wind energy accounts for 15% of the EU's electricity demand.

Due to major breakthroughs in wind power technology, wind turbines tend to be increasingly higher, with more capacity. This is because longer blades can take more wind, and taller turbines are able to capture stronger winds. While the early small turbines had capacities of around 20-60 kW, today's land-based supply is dominated by turbines in the 1.5-2 MW range [3]. Most turbine manufacturers are currently developing products with a capacity of 4.5-8 MW [4]. GE Renewable Energy is investing to develop the Haliade-X, the industry's largest 12 MW offshore wind turbine with a rotor diameter and height of 220 m and 260 m, respectively.

Both onshore and offshore wind turbines have advanced significantly. Especially the development of offshore wind energy has accelerated in the past few years. Offshore power projects have aroused great interest worldwide, in part because the winds over the oceans constitute significant resources. Yet also, because offshore turbines can address such issues as a lack of available land, inferior wind resources, as well as social and environmental concerns associated with onshore wind power projects [5]. The water depth of the offshore site is an important factor, as the turbine's foundation must be engineered for



Figure 1.1. Left : Curved-bladed Darrieus wind turbine [7], middle : Straight-bladed Darrieus wind turbine (picture from Vertical Wind AB), right : Savonius wind turbine [8]

that depth. The improved design of turbines and the development of floating substructures allow for economically competitive installation in deeper waters [6].

1.2 Wind turbine technologies

Wind turbines are classified into two general types: horizontal axis wind turbines (HAWTs) and vertical axis wind turbines (VAWTs). The former have a rotating axis parallel to the ground; the latter have an axis perpendicular to the ground. The HAWT is the common type in use today, and comes in a wide range of sizes and capacities. This type is used for its high capacity where constant wind is available. When the wind is turbulent, however, the HAWT cannot extract energy efficiently. The VAWT, on the other hand, is most suitable under these conditions.

To date, various VAWT designs have been introduced, as engineers have come up with ever new and innovative approaches to resolving issues associated with VAWTs, including low starting torque, blade fatigue caused by varying loads, low efficiency, poor building integration, etc. [9]. Two typical configurations are the Darrieus rotor and the Savonius rotor. Darrieus wind turbines have the highest values of efficiency among VAWTs, but they generally suffer from problems of low starting torque [9]. Lift force driven turbines, they produce the torque by the lift acting on the blades. The most common type of Darrieus turbine has curved ("egg-beater") blades, a shape designed to reduce the centrifugal stresses (Figure 1.1, left). Another type of Darrieus wind turbine, termed the H-rotor (also Giromill), has the egg-beater blades replaced with straight ones (Figure 1.1, middle). In the small-scale wind turbine market, the straight-bladed Darrieus is more cost effective than the egg-beater type [10]. The H-rotor is currently being actively investigated; among other

things, research is being done into the suitability of multi-megawatt turbines for offshore application [11]. Different from the lift-based Darrieus, the Savonius wind turbine is a drag-type device, consisting of two or more cup-shaped cylinders with a rotating shaft that can spin freely (Figure 1.1, right). In comparison with other types, the Savonius has low efficiency, but its advantages are its simplicity, robustness, and low cost [12].

The advantage of VAWTs over HAWTs is that they can absorb wind from any direction, without the need for yaw control. Requiring fewer mechanical components, the design is simpler. Also, as the main components, consisting of the generator and the gearbox, can usually be placed close to the ground, access for maintenance and repair is easy. In the case of floating offshore VAWTs, the generator can lower the center of gravity to platform level, thereby mitigating the cost of the floating structure. Furthermore, VAWTs generate lower noise emissions than HAWTs [13]. The Darrieus turbine produces more noise than the H-rotor, but less noise than a HAWT of the same size, since it rotates slower than the latter [14]. However, the efficiency of VAWTs is generally lower than that of HAWTs. This is partly because not all of the blades produce torque at the same time, so that other blades are simply pushed along. Yet it is also because VAWTs are usually built at ground level, where they cannot harness the higher wind speed available at higher altitudes. For these reasons, HAWTs currently dominate the market over VAWTs.

The operation of VAWTs involves complex and unsteady phenomena. For one thing, the variation of the relative wind speed which the blades experience during rotation complicates their aerodynamics. Also, the circular path of the blades gives rise to aerodynamic phenomena such as flow curvature and dynamic stall; the aerodynamics of static blades are different. Moreover, the blades in the downwind region inherently operate within the wake generated by the blades in the upwind and other components, i.e. a tower and struts. As a result, the torque in the downwind is lower as compared to that in the upwind, which directly affects the overall performance.

1.3 Wind turbine noise

One of the disadvantages of wind turbines is their noise emission during operation. Wind farms have been constructed in semi-rural areas close to major towns, in order to maximize electricity production and minimize transmission costs [15]. Yet the noise they generate is a serious issue for residents living nearby. Therefore, it is important to understand the mechanism of noise emission from wind turbines, so as to be able to mitigate the noise level as much as possible. Wind turbines have two main noise sources: mechanical and aerodynamic, as explained in the following.

1.3.1 Mechanical noise

Mechanical noise originates from machinery components such as the generator, yaw drives, and the gearbox. Various strategies for mechanical noise prevention or reduction exist, such as vibration suppression, vibration isolation, and fault detection techniques [16]. As manufacturers have succeeded in reducing the mechanical noise to a level below that of the aerodynamic noise, the latter now constitutes the dominant source of noise from wind turbines [17]. Due to the relative simplicity of VAWTs, the issue of mechanical noise may be largely left out of account.

1.3.2 Aerodynamic noise

Aerodynamic noise is generated by the blades passing through the air, and is mainly associated with the interaction of turbulence with the blade surface. The turbulence may originate either from the natural atmospheric turbulence in the incoming flow, or from the viscous flow in the boundary layer around the blades [17]. The sources of aerodynamic noise can be divided into airfoil self-noise, inflow-turbulence noise, and low-frequency noise. The total noise emission can be dominated by either airfoil self-noise or inflow-turbulence noise, depending on the configuration of the turbines and the operational conditions. Low-frequency noise is considered to be of minor importance for upwind turbines.

Airfoil self-noise

Airfoil self-noise is caused by the interaction between the blade and the turbulence in the boundary layer. This noise can have tonal and broadband character. Brooks et al. [18] distinguish five sources of airfoil self-noise:

- Trailing edge noise
- Laminar boundary layer vortex shedding noise
- Separation stall noise
- Blunt trailing edge noise
- Tip noise

Trailing edge noise is created by the turbulent boundary layer that develops on the blade surface passing the trailing edge of the turbine blade. Turbulent eddies in free space or on a flat wall are inefficient sound sources, but will become more efficient if there is a sharp edge close to the eddies [17]. The sound scattered at the trailing edge causes broadband noise and has characteristics of a dipole noise source. Laminar boundary layer vortex shedding noise occurs when a laminar boundary layer is present on one or both airfoil sides over the surface up to the trailing edge. Coupled to acoustically excited feedback loops between the trailing edge and an upstream point on the surface, where instability waves originate in the boundary layer, this source generates tonal noise [19, 20, 21]. Separation stall noise can arise in case of stall conditions. A

mildly separated flow causes sound emission from the trailing edge, whereas at deep stall condition, the noise is radiated from the chord as a whole [22]. Separation stall noise is a major noise source of wind turbines when the blades operate at high angles of attack and are fully separated for significant portions of time [23]. Blunt trailing edge noise is caused by vortices shedding from the blunt trailing edge. The noise level depends on the design of the blade; it can be mitigated by a sufficiently small thickness of the trailing edge. Tip noise is generated by the tip vortex, and is of broadband character. This noise is assumed to be influenced by the convection speed of the vortex and its spanwise extent [18].

Inflow-turbulence noise

It is considered that the key parameter affecting inflow-turbulence noise is turbulence intensity which is defined as the ratio of standard deviation of fluctuating wind velocity to the mean wind speed. Caused by the interaction between upstream atmospheric turbulence and the leading edge of the blades, it contributes mainly to broadband noise. The frequency of the radiated sound depends on the length scale of the disturbance in the atmosphere which can be much larger or smaller than the blade chord. Estimated to be a major source of aerodynamic noise in the frequency up to 1000 Hz, inflow-turbulence noise is not yet fully understood [17].

Low-frequency noise

Low-frequency noise is a dipole type loading noise, arising from the rotor-blades encountering the flow field generated by the tower. As the blades enter the flow field, the local angle of attack and the dynamic pressure change and cause a rapid change in blade loading. The interaction between the velocity fields of the tower and the blades gives rise to the discrete sound at low frequencies called low-frequency noise [17]. Its spectrum is dominated by the blade passing frequency and its harmonics.

1.4 Previous studies for wind turbine noise

Acoustic measurements for wind turbines have been conducted in numerous studies, either with the purpose of analyzing the noise level under different wind and operational conditions, or with the aim of identifying the sound sources of wind turbines. Migliore et al. [24] studied the acoustic emission of eight different small wind turbines for various wind speed. Rogers and Omer [25], and Buck et al. [26], assessed the effect of turbulent intensities on the noise levels of micro and large scaled HAWTs. Oerlemans et al. [27, 28] conducted field measurements for 850 kW and 2.3 MW HAWTs, using a microphone array to locate the sound sources. Their test results show that broadband trailing edge noise is the dominant noise source of these turbines, and

that the large noise level is produced during the downward movement of the blades, due to the convective amplification and trailing edge noise directivity. Möllerström et al. [29] and Ottermo et al. [30] performed noise measurements on a 200 kW VAWT. They found that most of the noise is generated in a narrow range of azimuth angle where high turbulence can be expected, as a noise contribution is observed at the position of the blade-strut joint. Pearson [31] carried out experiments for VAWTs using an acoustic array. The measured spectra showed a broadband peak around 1000 to 2000 Hz, which was considered to be caused due to laminar boundary layer tonal noise.

There are several theoretical studies which formulate wind turbine noise; most of these are based on semi-empirical models. Empirical models generally assume independently generated noise sources. Well-known models are those established by Grosveld [32] and Lowson [33] who proposed approaches for predicting the broadband noise of wind turbines by considering the contributions of inflow turbulence noise and trailing edge noise. Based on the model by Brooks et al. [18] for airfoil self-noise, and Lowson's model [33] for inflow turbulence noise, Moriarty and Migliore [23] developed the acoustic code for wind turbines. The code was validated against measurements for a full-scaled wind turbine. Zhu et al. [34] and Leloudas et al. [35] developed the empirical model to calculate the noise from large-scaled wind turbines.

Owing to recent advances in computing science, high fidelity computational fluid dynamics (CFD) simulations can be employed to directly solve the Navier-Stokes equations, as an alternative means of noise prediction. There exist some studies which compute the noise generated from HAWTs by CFD methods. Tadamasa et al. [36] predicted the noise radiated from the two-bladed HAWT using Reynolds-averaged Navier-Stokes (RANS) simulations, and the Ffowcs-Williams and Hawkings (FW-H) equation. They found that the loading noise is the dominant noise source up to a rotational speed of about 130 rpm, but that the thickness noise becomes dominant at higher rotational speed. Ghasemian and Nejat [37] presented the aero-acoustic prediction of the flow around the HAWT. They employed the improved delayed detached eddy simulation and the FW-H acoustic analogy to investigate the effect of the wind speed on the radiated noise. Maizi et al. [38] tested different tip blade configurations for the HAWT, to investigate their effect on the noise emission. They used RANS or detached eddy simulations in combination with the FW-H analogy, and showed that using a specific tip shape can reduce the sound pressure level.

Thus far, few studies using CFD methods for investigating noise from VAWTs have been reported. Among them is a study by Mohamed [39] in which two-dimensional RANS simulations were performed in order to examine to what extent the noise from Darrieus wind turbines depends on different blade shapes, tip speed ratios, and solidity. The simulations indicated that higher solidity and higher tip speed ratio rotors are more noisy. Ghasemian and Nejat [40] conducted the large eddy simulation (LES) to predict aerody-

namic noise radiated from the VAWT. They showed the dependency of the rotational speed on the strength of radiated noise level. Weber et al. [41] validated the numerical model based on an extended RANS model for a small-scaled Darrieus wind turbine. They found that the main noise source for the turbine operating at low tip speed ratio is caused by dynamic stall and the interaction between the blade in the downwind and the wake from the upwind side.

1.5 Contribution of this thesis

This thesis presents the noise prediction for the 12 kW three-bladed VAWT, using CFD simulations. Due to a lack of available acoustic measurement data, validation of noise prediction for VAWTs was insufficient. The prediction method was validated for the noise generated from a single static airfoil; this is presented in Paper I and II. The aerodynamics of the VAWT was simulated to characterize the flow fields at different tip speed ratios. The focus was placed on analyzing the influence of the struts on the blade forces that cannot be negligible when the force distribution along the blade needs to be accurately solved. Comparison was made as well for other numerical models, to assess the accuracy of each model for simulating the strut influence. This is presented in Paper III and IV. The aerodynamic noise for the VAWT was predicted and the results were validated using measurement data, which is presented in Paper V.

1.6 Outline of the thesis

Following the introduction, Chapter 2 outlines the theory of acoustic analogy, the spanwise correction method, and the basic aerodynamics of VAWTs. Chapter 3 gives a description of the VAWT studied in this thesis. The validation of the prediction method applied for a single airfoil case is addressed in Chapter 4. The aerodynamic and aeroacoustic studies for the VAWT are presented in Chapter 5 and Chapter 6, respectively. The final chapter summarizes the conclusions that can be drawn from the present studies, which is followed by suggestions for future research.

2. Theory

This chapter describes the theory of the acoustic analogy, which is applied to solve the sound propagation using the flow properties of the sound sources. The spanwise correction method is also explained which is used to estimate the total sound of the entire body from the sound sources of the limited section. The background theory of aerodynamics for wind turbines is summarized at the end.

2.1 Acoustic analogy

This section explains the theory of the Curle's analogy and the Ffowcs Williams and Hawkings (FW-H) analogy. The former is applicable for noise of static solid surfaces, while the latter is able to handle aeroacoustic sources of moving bodies in a fluid. These theories are used in Chapter 4 for a static blade case, and in Chapter 6 for the full VAWT case, respectively.

2.1.1 Curle's analogy

Lighthill [42] first proposed a generalization of the wave propagation equation for an arbitrary acoustic source region surrounded by a quiescent fluid. He derived the equation for the acoustic perturbations from mass and momentum conservation, assuming that there are no external forces acting on a fluid. Here the fluctuation of pressure and density are defined as $p' = p - p_0$ and $\rho' = \rho - \rho_0$ where p_0 and ρ_0 are constants in a reference fluid at rest far from the sound source. The derived equation, the so-called Lighthill's analogy, is written as

$$\frac{1}{c_0^2} \frac{\partial^2 p'}{\partial t^2} - \frac{\partial^2 p'}{\partial x_i^2} = \frac{\partial^2 T_{ij}}{\partial x_i \partial x_j} \quad (2.1)$$

where $T_{ij} = \rho u_i u_j + P_{ij} - c_0^2(\rho - \rho_0)\delta_{ij}$ is the Lighthill stress tensor, u_i is the fluid velocity in the i direction, $P_{ij} = p'\delta_{ij} - \tau_{ij}$ is the compressive stress tensor that includes the surface pressure and the viscous stress, c_0 is the speed of the sound in a reference fluid, δ_{ij} is the Kronecker delta. The right-hand side of Equation (2.1) represents the term of the sound source.

Curle [43] derived the solution of the Lighthill's equation for flows in the presence of static solid boundaries using the free space Green's function. The solution, called the Curle's analogy, is written as

$$p'(\mathbf{x}, t) = \frac{1}{4\pi} \frac{\partial^2}{\partial x_i \partial x_j} \int_V \frac{T_{ij}}{r} dV - \frac{1}{4\pi} \frac{\partial}{\partial x_i} \int_S \frac{n_p}{r} (p\delta_{ij} - \tau_{ij}) dS \quad (2.2)$$

where r is the distance between the sound source and the receiver and n_p is the unit vector normal to the surface. Equation (2.2) represents the sound pressure with integrals of the total volume external to the surface V and the surface of the boundaries S . The integrals are to be evaluated at the retarded time $\tau = t - r/c_0$ where t is time at the receiver. The spatial derivative can be converted as

$$\frac{\partial}{\partial x_i} = \frac{\partial}{\partial \tau} \frac{\partial \tau}{\partial x_i} = -\frac{1}{c_0} \frac{\partial r}{\partial x_i} \frac{\partial}{\partial \tau} = -\frac{h_i}{c_0} \frac{\partial}{\partial \tau} \quad (2.3)$$

where h_i is the unit vector pointing from the source location to the receiver in the i direction.

Larsson et al. [44] rewrote Equation (2.2) based on the formations by Brentner et al. [45]. The expression in equation (2.2) is modified to a form where the spatial derivative is converted to a temporal one using Equation (2.3) and the derivatives are taken inside the integral. Thus, $p'(\mathbf{x}, t)$ is expressed as

$$p'(\mathbf{x}, t) = \frac{1}{4\pi} \int_V \left(\frac{h_i h_j}{c_0^2 r} \ddot{T}_{ij} + \frac{3h_i h_j - \delta_{ij}}{c_0 r^2} \dot{T}_{ij} + \frac{3h_i h_j - \delta_{ij}}{r^3} T_{ij} \right) dV \\ + \frac{1}{4\pi} \int_S h_i n_p \left(\frac{\dot{p}\delta_{ij} - \dot{\tau}_{ij}}{c_0 r} + \frac{p\delta_{ij} - \tau_{ij}}{r^2} \right) dS \quad (2.4)$$

where dots such as \dot{p} indicate a derivative with respect to time. In this study, the term for the volume integral, which represents quadrupole source terms, is neglected and only the second term, which corresponds to the dipole sound source generated by the force on the surface, is considered. This is because the contribution of the quadrupole sources to the total sound is generally expected to be much smaller than those of the monopole and dipole sources for flows in low Mach number regime [46]. Also, it can be assumed in almost all cases that the surface source term is determined by the surface pressure and the viscous stresses on the surfaces τ_{ij} is negligible [47]. Thus, the sound pressure used in this study is reduced to as

$$p'(\mathbf{x}, t) = \frac{1}{4\pi} \int_S \left(\frac{h_i n_p \dot{p}}{c_0 r} + \frac{h_i n_p p}{r^2} \right) dS \quad (2.5)$$

2.1.2 Ffowcs Williams and Hawkings analogy

The Ffowcs Williams and Hawkings (FW-H) equation is an extension of the equation developed by Lighthill and describes the sound generated by a body

moving in a fluid represented as a moving control surface. The FW-H equation for p' is written as

$$\begin{aligned} \frac{1}{c_0^2} \frac{\partial^2 p'}{\partial t^2} - \frac{\partial^2 p'}{\partial x_i^2} = \frac{\partial}{\partial t} \left\{ [\rho_0 v_n + \rho(u_n - v_n)] \delta(f) \right\} \\ - \frac{\partial}{\partial x_i} \left\{ [P_{ij} n_j + \rho u_i (u_n - v_n)] \delta(f) \right\} + \frac{\partial^2}{\partial x_i \partial x_j} \{ T_{ij} H(f) \} \end{aligned} \quad (2.6)$$

where u_n is the fluid velocity in the direction normal to the surface, v_n is the velocity of the surface, n_j is the unit vector in the j direction, $\delta(f)$ is the Dirac delta function, $H(f)$ is the Heaviside function, respectively. The shape and the motion of the control surface is described using f , i.e. $f > 0$ implies outside the surface, $f = 0$ the body surface, and $f < 0$ inside the surface.

The first term on the right hand side of Equation (2.6) relates the monopole type source, and the thickness noise can be represented by this. The second term relates the dipole type source, and the loading noise originates from this term. The third term relates the quadrupole type source and is assumed negligible here as was done in many subsonic applications.

The solution can be obtained using the free space Green's function. The sound pressure at a receiver position can be written as the summation of the thickness and loading noise:

$$p' = p'_T + p'_L \quad (2.7)$$

The thickness noise p'_T is

$$\begin{aligned} 4\pi p'_T(\mathbf{x}, t) = \int_{f=0} \left[\frac{\rho_0(v_n n_p + v_n n_p)}{r(1 - M_r)^2} \right]_{ret} dS \\ + \int_{f=0} \left[\frac{\rho_0 v_n n_p \{ r r_i \dot{M}_i + c_0 (M_r - M_i^2) \}}{r^2 (1 - M_r)^3} \right]_{ret} dS \end{aligned} \quad (2.8)$$

and the loading noise p'_L is

$$\begin{aligned} 4\pi p'_L(\mathbf{x}, t) = \frac{1}{c_0} \int_{f=0} \left[\frac{\dot{l}_i r_i}{r(1 - M_r)^2} \right]_{ret} dS + \int_{f=0} \left[\frac{l_r - l_i M_i}{r^2 (1 - M_r)^2} \right]_{ret} dS \\ + \frac{1}{c_0} \int_{f=0} \left[\frac{r l_r r_i \dot{M}_i + c_0 l_r (M_r - M_i^2)}{r^2 (1 - M_r)^3} \right]_{ret} dS \end{aligned} \quad (2.9)$$

where r_i is the unit vector pointing from the source location to the receiver, $l_i = p n_p$ is the pressure vector exerted by fluid on the surface, $l_r = r_i l_i$ is the component of l_i in the direction of radiation, $M_i = v_n / c_0$ is the Mach number at a point on the surface, $M_r = r_i v_n / c_0$ is the Mach number for the velocity component in the radiation. The subscript *ret* denotes that the integrand is evaluated at the retarded time τ . The detail description of the derivation can be found in Farassat [48].

Since the dominant wavelength of the generated sound is typically much larger than the dimensions of the flow unsteadiness at low Mach numbers [49], the sound source is regarded as compact in this study. It can also be assumed at low Mach number that the sound radiation from a flow can be calculated using the incompressible flow [50]. The formulation takes into account the compressibility in the flow region, but the use of an incompressible solver is appropriate if the interaction between turbulence and body surface occurs in a region that is compact enough to have minor diffraction effect [51].

2.2 Spanwise correction

The spanwise correction is necessary because of high computational cost for fully simulating total sound sources, so the correction is applied in Chapter 4 for the single blade case to estimate the total sound pressure from the sound sources of a limited blade surface area. In this section, the spanwise correction method proposed by Seo and Moon [52] is briefly explained. They proposed a noise prediction methodology for long-span bodies by revisiting a simple correction suggested by Kato et al. [53] and Pérot et al. [54].

Here we denote the sound pressure generated from the total and simulated span sections L and L_s as p'_{all} and p'_s , respectively. If the sound source occurs along the span independently in the statistical sense, the sound power can be approximated to be proportional to the span length, i.e. $p'^2_{all}/p'^2_s \propto L/L_s$. If the pressure fluctuates in phase along the span, the sound power can be assumed to be proportional to the squared span length, i.e. $p'^2_{all}/p'^2_s \propto L^2/L_s^2$ [55]. The spanwise correction method also defines how to approximate p'_{all} when the degree of coherence of the sound source is in between the two extreme cases.

The sound pressure level (SPL) is defined as

$$\text{SPL} = 10 \log_{10} \left(\frac{p'}{p_{ref}} \right)^2 \quad (2.10)$$

where the reference pressure p_{ref} is the threshold of human hearing, 2×10^{-5} Pa. Let us denote the SPL generated from the sections L and L_s as SPL_{all} and SPL_s . So,

$$\text{SPL}_{all} = \text{SPL}_s + \text{SPL}_{cor} \quad (2.11)$$

where SPL_{cor} is the SPL needed for correction. SPL_{cor} is defined as a function of frequency f :

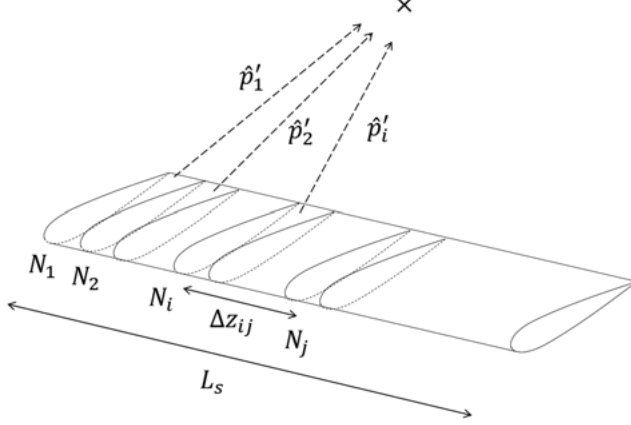


Figure 2.1. Schematic of the subdivided blade for spanwise correction

$$\text{SPL}_{cor}(f) \equiv$$

$$\begin{cases} 20\log\left(\frac{L}{L_s}\right) & \left(\frac{L}{\sqrt{\pi}L_s} \leq \frac{L_c}{L_s}\right) & (2.12a) \\ 10\log\left(\frac{L_c}{L_s}\right) + 10\log\left(\frac{\sqrt{\pi}L}{L_s}\right) & \left(\frac{1}{\sqrt{\pi}} < \frac{L_c}{L_s} < \frac{L}{\sqrt{\pi}L_s}\right) & (2.12b) \\ 10\log\left(\frac{L_c}{L_s}\right) & \left(\frac{L_c}{L_s} \leq \frac{1}{\sqrt{\pi}}\right) & (2.12c) \end{cases}$$

where L_c , a function of f , is the spanwise coherence length determined from the spanwise coherence function. The correction is made based on the degree of the spanwise coherence of the turbulence structures. Equation (2.12a) is used if the pressure fluctuation occurs in phase, and Equation (2.12c) is used if the pressure fluctuates inhomogeneously. Equation (2.12b) is applied when the phase difference falls into the range between these two cases.

The coherence length L_c is calculated as follows. Consider the case where the blade of span length L_s is divided into N subsections in the spanwise direction as shown in Figure 2.1. The power spectral density of sound pressure radiated from a subsection N_i is denoted as \hat{p}'_i . The sound pressure radiated from each subsection is lagged by a phase difference which can be characterized by the coherence function:

$$\gamma'_{ij}(f, \Delta z_{ij}) = \frac{\overline{\text{Re}(\hat{p}'_i \hat{p}'_j^*)}}{\sqrt{|\hat{p}'_i|^2} \sqrt{|\hat{p}'_j|^2}} \quad (2.13)$$

This is a function of the distance between two subsections, Δz_{ij} . Since the phase lagging in the spanwise direction tends to follow a Gaussian distribu-

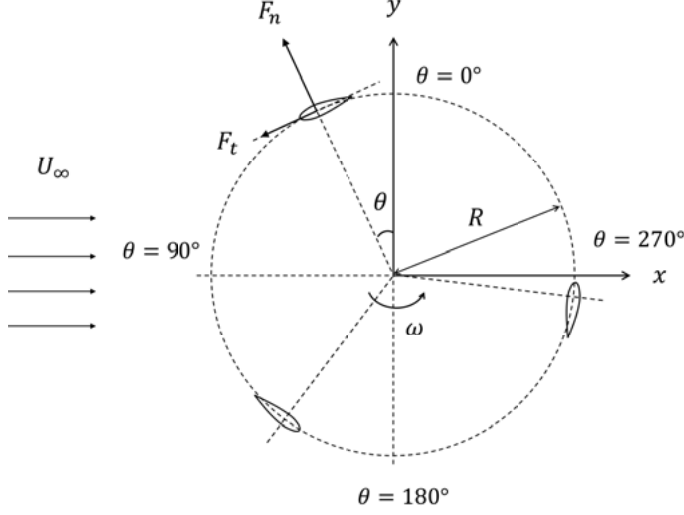


Figure 2.2. Azimuthal coordinates of the rotational plane

tion [56], the acoustic spanwise coherence function $\gamma'(\Delta z)$ can also be expressed as

$$\gamma'(f, \Delta z) = \exp\left(-\frac{\Delta z^2}{L_c^2}\right) \quad (2.14)$$

The value of L_c is determined which satisfies to best fit the Gaussian distribution function γ' in Equation (2.14) for a set of $\Delta z_{i,j}$ and $\gamma'_{i,j}(\Delta z_{i,j})$ obtained in Equation (2.13). The detailed theory is explained in Seo and Moon [52].

2.3 Basic aerodynamics of wind turbines

The theory of aerodynamics for wind turbines is summarized in this section. The top view of the rotor with radius R rotating at angular velocity ω is shown in Figure 2.2. U_∞ represents the freestream velocity at hub height. The azimuth angle is denoted by θ . The tip speed ratio λ is defined as

$$\lambda = \frac{R\omega}{U_\infty} \quad (2.15)$$

A VAWT must slow down the incoming wind speed in order to transform kinetic energy in the wind to useful power, and a thrust force that exists with a direction opposite to the wind is responsible for an induced velocity at the rotor [57]. The relative velocity \mathbf{U}_{rel} seen by the blade determines the aerodynamic force and is expressed by the sum of the induced velocity at the blade

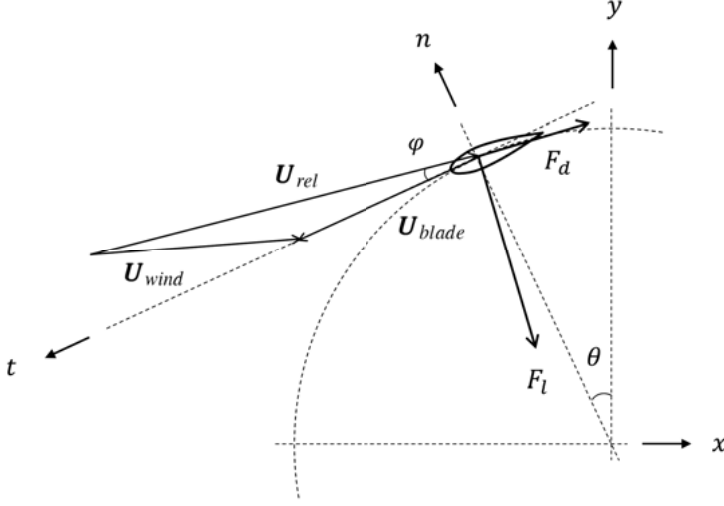


Figure 2.3. Schematic of the relative wind speed at blade position

position \mathbf{U}_{wind} and the inverse of the blade velocity \mathbf{U}_{blade} , as shown in Figure 2.3. Thus,

$$\mathbf{U}_{rel} = \mathbf{U}_{wind} - \mathbf{U}_{blade} \quad (2.16)$$

The angle of relative wind φ is expressed as

$$\tan \varphi = \frac{U_{rel,n}}{U_{rel,t}} = \frac{U_{wind,n}}{U_{wind,t} - U_{blade,t}} = \frac{U_{wind,x} \sin \theta - U_{wind,y} \cos \theta}{R\omega + U_{wind,x} \cos \theta + U_{wind,y} \sin \theta} \quad (2.17)$$

where the normal and tangential components of each vector are represented with the subscripts of n and t , and the x and y components are represented with the subscripts of x and y . The angle of relative wind when the wind is undisturbed, denoted as φ_0 , can be expressed more simply using λ as

$$\tan \varphi_0 = \frac{\sin \theta}{\lambda + \cos \theta} \quad (2.18)$$

The angle of relative wind φ is the summation of the angle of attack α and the blade pitch angle γ_{pitch} , so

$$\varphi = \alpha + \gamma_{pitch} \quad (2.19)$$

The lift and drag forces F_l and F_d are produced, which are perpendicular and parallel to the direction of \mathbf{U}_{rel} , respectively. The normal and tangential forces F_n and F_t that are illustrated in Figure 2.2 can be expressed using F_l and F_d as

$$F_n = -F_l \cos \varphi - F_d \sin \varphi \quad (2.20)$$

$$F_t = F_l \sin \varphi - F_d \cos \varphi \quad (2.21)$$

The positive values of F_n and F_t are defined to be in the outward and the rotational directions, respectively.

Average tangential force \bar{F}_t on one blade during revolution is obtained as

$$\bar{F}_t = \frac{1}{2\pi} \int_0^{2\pi} F_t d\theta \quad (2.22)$$

and the total torque T for the number of blades N_B can be calculated as

$$T = N_B \bar{F}_t R \quad (2.23)$$

For VAWTs whose blades are supported by struts, such as the H-rotor, the strut also contributes to the total torque. The total power P can be obtained as

$$P = T\omega \quad (2.24)$$

The power coefficient C_p is an indicator of how efficiently the wind turbine converts the energy in the wind into electricity. C_p is defined as

$$C_p = \frac{P}{P_{wind}} = \frac{P}{\frac{1}{2}\rho AU_\infty^3} \quad (2.25)$$

where P_{wind} is the kinetic energy available in the wind that passes through the swept area of the rotor A with the velocity U_∞ . The theoretical maximum value of C_p for HAWTs is around 59.3 %, which is known as the Betz limit. Some literature claim that this limit might not be applicable to VAWTs. The turbine should be operated at optimal tip speed ratio where the power absorption is maximized, i.e. the possible highest C_p . At low tip speed ratio, the blades undergo dynamic stall due to the large angle of attack variation and C_p drops down. At very high tip speed ratio, the rotor runs so fast that the wind flow is blocked by the rotor, so there is little energy that can be extracted. The tip speed ratio should also not be too high to withstand structural loads and avoid being noisy.

3. Description of the 12 kW vertical axis wind turbine at Marsta

At the Division of Electricity at Uppsala university, wind power research has been conducted since 2002, with three VAWTs designed and built as part of the project. One of these turbines is the straight bladed 12 kW H-rotor located in the north of Uppsala at Marsta, shown in Figure 3.1. Various measurements for this turbine have been performed [58, 59, 60, 61], and several simulation tools have been developed [62, 63, 64, 65]. This thesis furthermore investigates its aerodynamics.

The main parameters of the geometry are listed in Table 3.1. The radius of the rotor is $R = 3.24$ m, and the hub is located at 6 m from the ground. It consists of three blades which have the cross-sectional profile of a NACA 0021 airfoil. Each blade has a length of $H = 5$ m. The chord length is $c = 25$ cm, and is tapered on both sides, starting from 1 m at the blade tip, with the chord linearly decreasing to 15 cm at the tip. The Reynolds number based on chord length varies in the range of the order of 10^5 during revolution. As shown in Figure 3.2, two inclined struts are attached to each blade at 27 % of the blade length from both ends, with the mounting angles of $\pm 17.6^\circ$ relative to the horizontal plane. While the dominant force of horizontal struts is drag, the struts of this VAWT are jointed with an angle and therefore can produce lift. The cross-section of the struts is designed based on a NACA 0025 profile, but with modification at the trailing edge to have a blunt edge. The chord length varies linearly from 32 cm at the root up to 20 cm at the attachment point.



Figure 3.1. The 12 kW vertical axis wind turbine at Marsta

Table 3.1. *Parameters of VAWT*

Rated power	12 kW
Number of blades	3
Radius	3.24 m
Hub Height	6 m
Blade length	5 m
Blade profile	NACA 0021
Chord length at center	0.25 m
Chord length at tip	0.15 m
Blade pitch angle	2°
Strut profile	NACA 0025
Strut tip chord	0.2 m
Strut root chord	0.32 m
Strut root attachment point from center	0.2 m
Strut tip attachment point from center	1.15 m

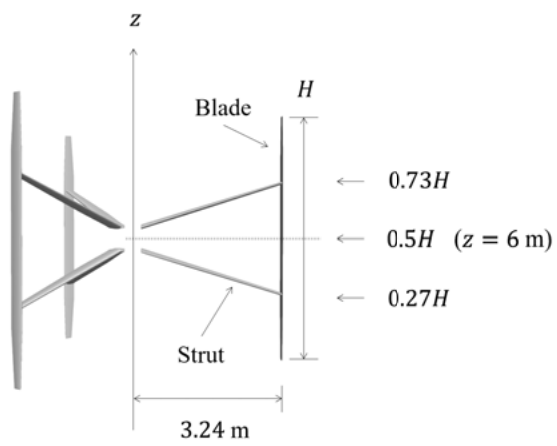


Figure 3.2. Height of the blade and struts

4. Validation of noise prediction

This chapter deals with the validation of the method of noise prediction. The validation is based on the hybrid approach, using CFD simulation and the acoustic analogy for noise prediction. The validation is made for a single static airfoil in stall condition. Since high resolution of the mesh is required to calculate the sound sources in CFD simulations, the computational domain size is limited and may not be large enough to capture the full turbulence flow structure. Therefore, the spanwise correction method is used in which the simulated flow properties related to the sound source are statistically extrapolated to calculate the noise generated from the entire span section.

4.1 Study case

The numerical method is validated by comparing the measurement conducted by Brooks et al. [18] for the noise radiated from a single static blade. They recorded the self-noise of a NACA 0012 airfoil placed in an anechoic wind tunnel. The chord length of the blade is $c = 10.16$ cm and the span length is $L = 45$ cm. The freestream velocity is $U_0 = 71.3$ m/s, which leads to the condition that the Reynolds number based on the chord length is 4.8×10^5 and the Mach number is 0.2. This study investigates the airfoil with 15.6° angle of attack, which is expected to be in the stall region. The sound is received at 1.2 m perpendicular to the trailing edge of airfoil in the midspan plane, and the published data are provided as one-third octave band spectra.

The experimental setup using the wind tunnel can create downwash deflection of the incident flow. In the measurement, two side plates are flush mounted on the jet nozzle lip and the airfoil model is held between the plates. The proximity of the airfoil to the jet nozzle and the limited jet width can cause the airfoil pressure loading and flow characteristics to deviate from those measured in free air [66], which effectively reduces the angle of attack.

The effective angles of attack, denoted by α_* , are examined using RANS simulations where the full wind tunnel setup is reproduced including the jet nozzle, the entire airfoil model, and the side plates. The simulated velocity field shows the flow curvature caused by the downwash effect, and the effective angles of attack are calculated from the velocity deflected in the wake. Brooks et al. [67] use the lifting surface theory to correct the geometrical angles of attack. The effective angles α_* obtained by the RANS simulations and the lifting theory are plotted in Figure 4.1 against the geometrical angles α_t .

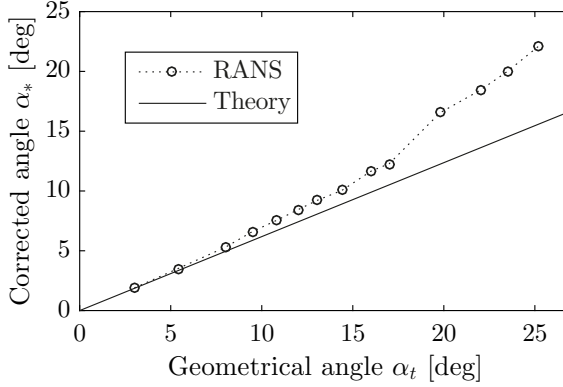


Figure 4.1. Effective angles of attack obtained from the RANS simulations (dotted line) and the lifting surface theory (solid line) against the angles of attack referenced to streamwise axis

While α_* obtained in the simulation are close to the theoretical values up to around $\alpha_t = 16^\circ$, the simulated values of α_* deviate largely from the theory at high α_t . Therefore, it can be considered that the lifting surface theory is valid only for attached flows and is not well suitable to apply to angles in the post-stall regime. For this reason, the prediction of noise for airfoil with 15.6° angle of attack is validated using the data measured with 19.8° angle of attack. More detailed procedure for determination of the effective angle of attack can be found in Paper I.

4.2 Numerical method

Incompressible flow around the airfoil is solved using LES, and then the Curle's analogy is applied to calculate the sound propagation. The flow simulations are performed using an open source code OpenFOAM [68], which solves the continuity and momentum equations based on the finite volume method. As a subgrid-scale (SGS) model, one equation eddy viscosity model [69] is used where the SGS eddy viscosity is expressed by the SGS kinetic energy and the grid width. The transport equation for the SGS kinetic energy is solved every step.

The PIMPLE algorithm, which was developed for transient problems, is applied to solve the coupled pressure-velocity equations, where the pressure-velocity coupling is recalculated in one time step. The second-order schemes are used for both the spatial and temporal discretization.

Figure 4.2 shows the computational domain and the boundary conditions. A NACA 0012 airfoil with chord length c is located at the origin. The simulated airfoil has a span length $L_s = 0.4c = 4.46$ cm. This size is 10 % of the span length of the experimental model that is $L = 45.72$ cm. The solid wall condi-

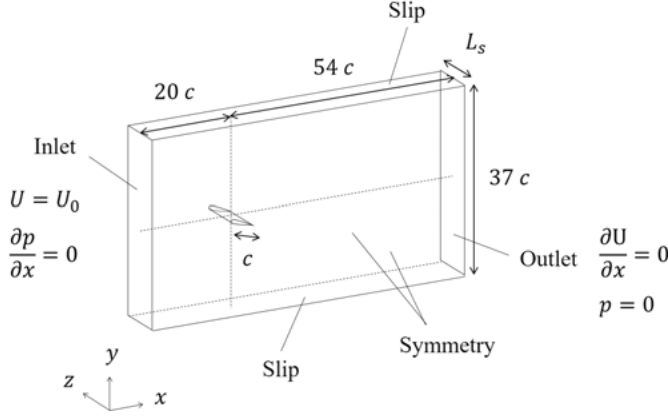


Figure 4.2. Computational domain and boundary conditions

CASE	L_s	Number of mesh points	BC	Duration of simulated time steps
A	$0.4c$	49 million	Symmetry	0.0535 sec
B	$0.4c$	16 million	Symmetry	0.2095 sec
C	$0.4c$	16 million	Periodic	0.1654 sec
D	$1.3c$	47 million	Symmetry	0.0626 sec
E	$1.3c$	47 million	Periodic	0.0844 sec

Table 4.1. Five test cases studied in this paper

tion is used on the airfoil surface where the boundary layer is solved without using the wall functions.

Five cases are examined as listed in Table 4.1. A reference test case is represented as CASE A. It is necessary to ensure that the simulated span extent L_s is sufficient to correct for the total noise. Thus, two cases are run with the same domain size $0.4c$ (CASE B) and three-times larger size $1.3c$ (CASE D). While the symmetry boundary condition is applied in the reference case, the periodic condition is tested as well. Two cases using the periodic condition with different domain sizes, $0.4c$ and $1.3c$, correspond to CASE C and CASE E, respectively.

The flow domain is discretized using structured grids. The mesh used in CASE A consists of 49 million cells. The geometry of an airfoil configuration is meshed with approximately 1134 and 257 points along the chord and span, respectively. Figure 4.3 shows the zoomed view of the mesh around the airfoil. The grid spacing in the direction normal to the wall y^+ is below unity for the mesh of CASE A on the airfoil surface. The coarse mesh which has double spacing is used from CASE B to CASE E to complete simulations in reasonable computational time.

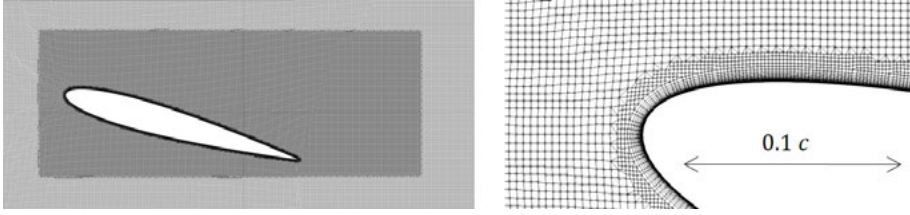


Figure 4.3. Zoomed view of the discretized mesh around airfoil

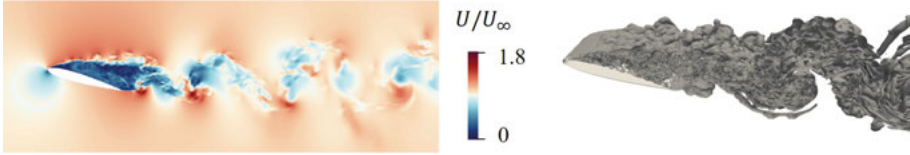


Figure 4.4. Instantaneous velocity field (left) and isocontour for the magnitude of vorticity of 5000 s^{-1} (right)

4.3 Results and discussion

The primary results for the simulated flow field around the airfoil are summarized in this section. Using the flow properties obtained by LES, the sound at the observation point is predicted based on the acoustic analogy. After the procedure for calculation of the spanwise correction is explained, the predicted total noise is compared with measurement data.

4.3.1 Flow characteristics

Figure 4.4 shows the instantaneous velocity field around the airfoil and the isocontour of the vorticity. The pictures to the left and right depict the magnitude of velocity \mathbf{U} normalized with U_0 and the isocontour for the magnitude of the vorticity $|\nabla \times \mathbf{U}| = 5000 \text{ s}^{-1}$, respectively. It can be observed that the flow is separated from the leading edge, and that large-scaled vortices are shed from the whole surface on the suction side. The velocity sampled in the wake indicates that the vortices are generated at around 497 Hz. Small vortices can also be seen in the shear layer close to the leading edge.

Figure 4.5 shows the time derivative of the pressure \dot{p} on the airfoil surface. The values depicted are scaled with the range of $\dot{p} = \pm 1.5 \times 10^6 \text{ Pa/s}$. This illustrates that \dot{p} behaves differently depending on the chord location. The pressure fluctuates with small-scaled structures at the rear of the airfoil, while in the front half of the airfoil the wavelike change occurs which is highly constant along the span.

Figure 4.6 shows the power spectral density of the pressure fluctuation at chordwise locations of 0, $0.2c$, $0.5c$, $0.95c$ on the suction and $0.95c$ on the pressure sides. The spectral density in dB per Hz is calculated with the ref-

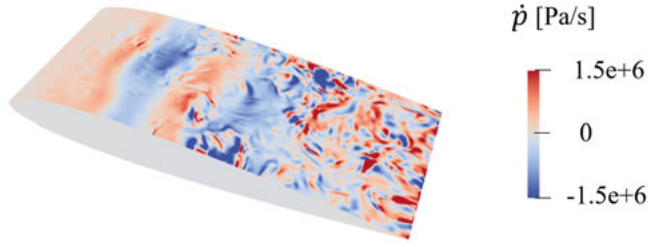


Figure 4.5. Time derivative of surface pressure \dot{p}

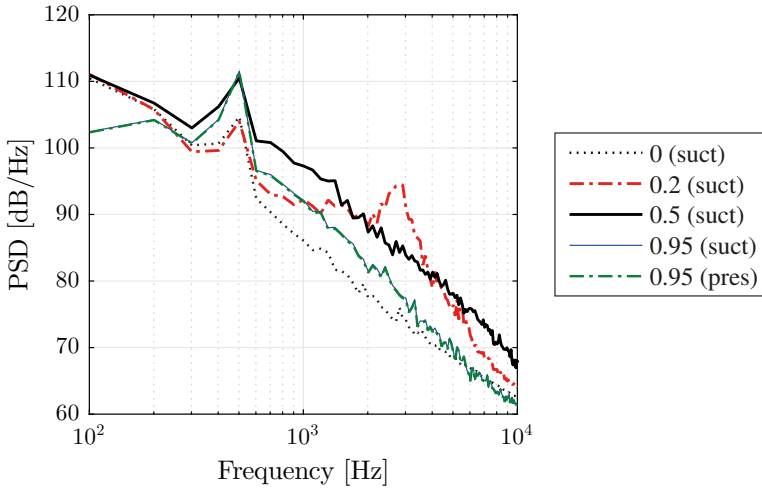


Figure 4.6. Power spectral density of the surface pressure fluctuation at chordwise locations of 0, 0.2c, 0.5c, 0.95c on the suction and 0.95c on the pressure sides with reference to 2×10^{-5} Pa

erence pressure of $p_{ref} = 2 \times 10^{-5}$ Pa. The dominant peaks are clearly seen at 502 Hz at all chordwise locations, and it is considered that these peaks are caused due to large vortices shed in the wake. There is a second peak at 2913 Hz for the location of 0.2c with the lower amplitude. In Figure 4.5, the wave pattern of the surface pressure derivative \dot{p} is observed in the front half of the airfoil. The velocity sampled in the region where vortices are formed in the shear layer close to the leading edge indicates that the shedding frequency is between 2500 Hz and 3000 Hz, and it can be considered that these leading edge vortices yield the peak at 2913 Hz in the spectrum. The power spectra also indicate that the surface pressure at the location of 0.5c is highest at almost all frequencies except at around 2913 Hz. The pressure at 0.95c has close amplitude on both airfoil sides.

4.3.2 Verification for spanwise correction

The noise radiated from the total span L is calculated using the spanwise correction method proposed by Seo and Moon [52] in which the SPL from the limited domain size is corrected based on the degree of correlation of the turbulence structure along the span. Most of previous studies which predict noise for an airfoil at low angle of attack simply assume the homogeneous turbulence of the sound source, as the flow is mostly attached over the airfoil surface. However, when the airfoil is in the stall region, the flow around the airfoil generates large-scaled vortices in the wake, which can be the main noise source of a long wavelength at low frequency. A large domain size in the spanwise direction is then needed to capture the full vortex structures. Therefore, the spanwise correction is applied here to reduce computational cost. The procedure of calculating the SPL for correction, SPL_{cor} , is explained as follows.

The span of airfoil is divided into 5 subsections, N_1, \dots, N_5 (see Figure 2.1). Both ends of length $L_s/12$ are not used to avoid including the boundary effect. FFT is performed for the sound pressure radiated from each subsection. Then, the auto power spectra for $\hat{p}'_1, \dots, \hat{p}'_5$ and the cross spectra between \hat{p}'_i and \hat{p}'_j for all combinations of i and j ($i, j = 1, \dots, 5, i \neq j$) are calculated. The coherence functions $\gamma'_{i,j}$ are obtained as a function of the distance $\Delta z_{i,j}$ at each frequency. $L_s(f)$ is the parameter of the Gaussian distribution function γ' which is determined by applying the least-square fitting to a set of the data points $\Delta z_{i,j}$ and $\gamma'_{i,j}$.

Figure 4.7 shows the coherence functions γ' at three selected frequencies, 299 Hz, 524 Hz, and 748 Hz, when they are viewed as a function of the spanwise distance. The simulated span extent L_s corresponds to $\Delta z/L = 0.1$. The four data points $\Delta z_{i,j}$ and $\gamma'_{i,j}$ for each frequency are depicted with markers. The curve lines represent γ' obtained by the best fitting, showing the decay of the coherence as the distance increases. The coherence function at 524 Hz, which is close to the frequency of vortex shedding in the wake, remains high and is larger than 0.9 even at $\Delta z/L = 0.1$. By contrast, the curve at 748 Hz indicates a rapid decrease within the distance of the simulated span length.

The value of SPL_{cor} is obtained based on Equation (2.12a–2.12c) using the coherence length L_c for each frequency. Figure 4.8 shows L_c normalized with L_s as well as SPL_{cor} . In this study case, SPL_{cor} becomes the maximum of 20 dB if L_c/L_s is larger than 5.8, while SPL_{cor} becomes the minimum of 10 dB if L_c/L_s is smaller than 0.6. The results show that the coherence length is large and SPL_{cor} becomes almost maximum at around the vortex shedding frequency. Then, SPL_{cor} sharply decreases and becomes close to the minimum value at high frequencies larger than 1000 Hz.

Two cases, CASE B and CASE D, are tested in order to verify that the present spanwise domain size is sufficient to apply the spanwise correction method. Figure 4.9 shows the spectra of the SPL before and after correction,

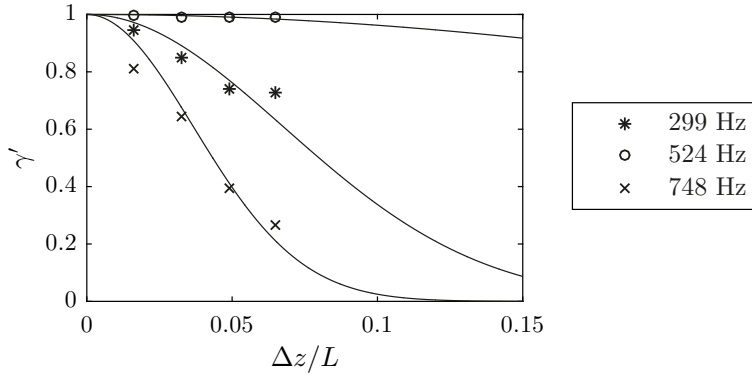


Figure 4.7. Coherence function γ' at three selected frequencies, 299 Hz, 524 Hz, and 748 Hz plotted against normalized spanwise distance $\Delta z/L$

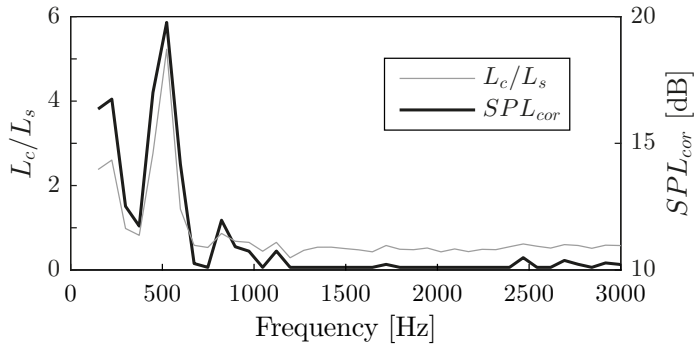


Figure 4.8. Spanwise coherence length L_c normalized with L_s and the sound pressure level for correction SPL_{cor}

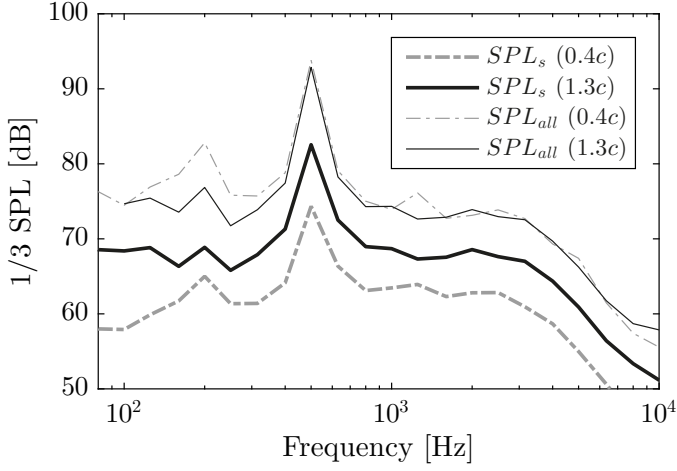


Figure 4.9. 1/3 octave band spectra for the SPL simulated using the spanwise domain sizes of $0.4c$ (CASE B, dotted grey) and $1.3c$ (CASE D, solid black) observed at 1.2 m from the trailing edge with reference p_{ref} . Both the SPL before correction (SPL_s) and after correction (SPL_{all}) are shown for each case.

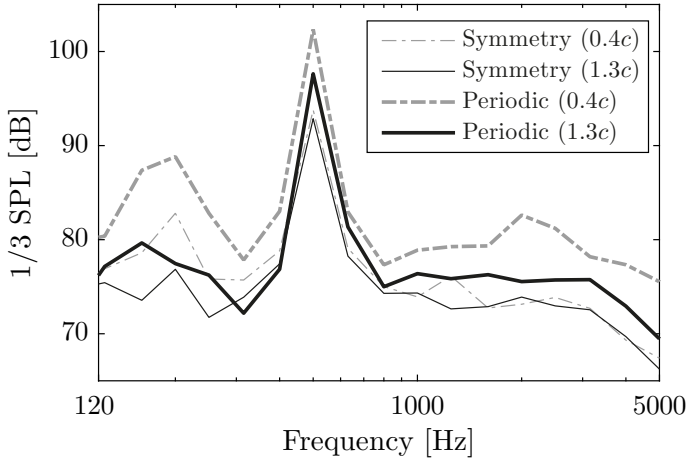


Figure 4.10. Spectra of the corrected SPL simulated using the symmetry and periodic boundary conditions with the spanwise domain sizes of $0.4c$ and $1.3c$

SPL_s and SPL_{all} , for the two cases. The sound spectra are represented in one-third octave frequency bands with the reference pressure of p_{ref} for this and all figures that follow in the thesis. The corrected SPL of the two cases converges closely in the range of frequencies higher than 400 Hz, which indicates that the correction method is applicable to the dimension of the spanwise domain $L_s = 0.4c$ so as to reproduce the total SPL. The large discrepancy is seen at frequencies around 200 Hz. This is likely to arise due to the finite computational domain that can create spurious sound of the wavelength of the same length as the domain size.

4.3.3 Influence of boundary condition

Two different boundary conditions in the spanwise direction, namely, the symmetry and periodic conditions, are tested to examine their influence on the predicted sound. Figure 4.10 shows the corrected SPL for CASE B to CASE E, i.e. the cases simulated using the symmetry and periodic conditions with the spanwise domain sizes of $0.4c$ and $1.3c$. Unlike the symmetry cases, the corrected SPL of the two periodic cases do not converge to close values each other. This indicates that the domain size in the spanwise direction can affect the flow properties related to acoustic sources when the periodic condition is applied, and thus a longer span length might be needed to be acoustically independent from the boundary effect.

4.3.4 Comparison with measurement

Figure 4.11 shows a comparison between the SPL as predicted by LES, and measured by Brooks et al. [18]. The SPL corrected with the maximum value of $SPL_{corr} = 20$ dB and the minimum value of 10 dB are depicted as well. The simulation is able to predict the frequency of the main peak at 500 Hz that can be considered to be caused by the vortex shedding in the wake, but does not reproduce the shape of the moderate hump highly accurately. This might be improved by using a finer mesh, as for example Singer et al. [70] state that increasing the grid resolution fills the spectrum more fully. Although there is a distinctive frequency of the surface pressure at 2913 Hz in the front half of the airfoil observed in Figure 4.6, this high frequency component does not yield a noticeable noise level in the spectrum.

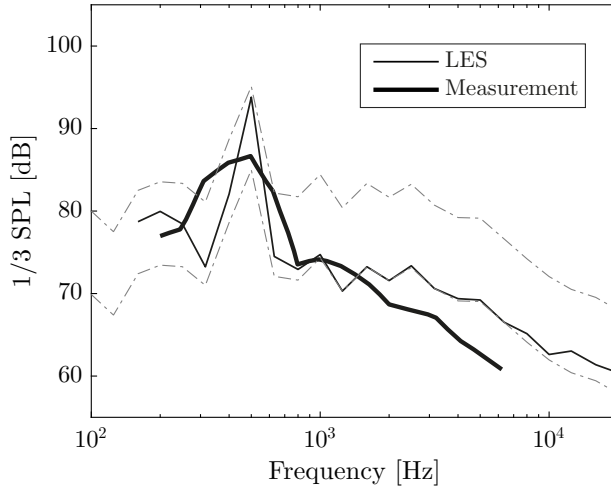


Figure 4.11. 1/3 octave band spectra for the total SPL corrected for the entire span (thin line) and the SPL measured by Brooks et al. [18] (bold line) observed at 1.2 m from the trailing edge with reference p_{ref} . The SPL corrected with the maximum and minimum values of SPL_{corr} (dashed line) are presented as well.

5. Aerodynamic studies for vertical axis wind turbine

This chapter highlights the importance of modeling the strut effect for accurate prediction of the aerodynamics of the VAWTs. In the case of the H-rotor turbine, the wake generated by the struts can influence the blade forces significantly. Although it is well-known, most of numerical studies do not consider strut components due to high computational cost. The influence of the struts is relevant also to acoustic prediction, where the detailed flow behavior around the blade surface needs to be calculated. Flow disturbance around the joint between the blade and struts can also be a contributing factor to the noise source.

The actuator line model (ALM) and the vortex model are numerical approaches widely employed today for simulating flows of VAWTs, along with the CFD model. All three approaches are studied here, so as to compare their performance for accurately modeling the strut effect. First, the numerical method for the CFD model using RANS simulations is explained, followed by the validation of the CFD model. Simulations are performed using each model for different tip speed ratios. Finally, the main results are discussed and presented.

5.1 Numerical method

The technique of the ALM is to solve the Navier-Stokes equations, but to replace the actual geometry with lines carrying body forces. The ALM requires the lift and drag coefficients. Two sources of these coefficients are considered, one reported by Sheldahl and Klimas [71], the other obtained from the XFOIL program [72], henceforth denoted as ALM-SK and ALM-XF, respectively. The vortex method formulates the Navier-Stokes equations in terms of vorticity. More detailed descriptions of the ALM and the vortex model can be found in Paper IV.

Unlike the ALM and the vortex method which only work for airfoil profiles with known force coefficients, the advantage of the CFD approach is its capability of fully solving the boundary layer of the blade surface without any approximation of the geometry of structure. Thus, it is suitable when the aerodynamic characteristics of VAWTs need to be captured with high precision.

In the CFD model, three-dimensional incompressible flow is solved by RANS simulations with the SST $k - \omega$ turbulence model [73]. This turbulence

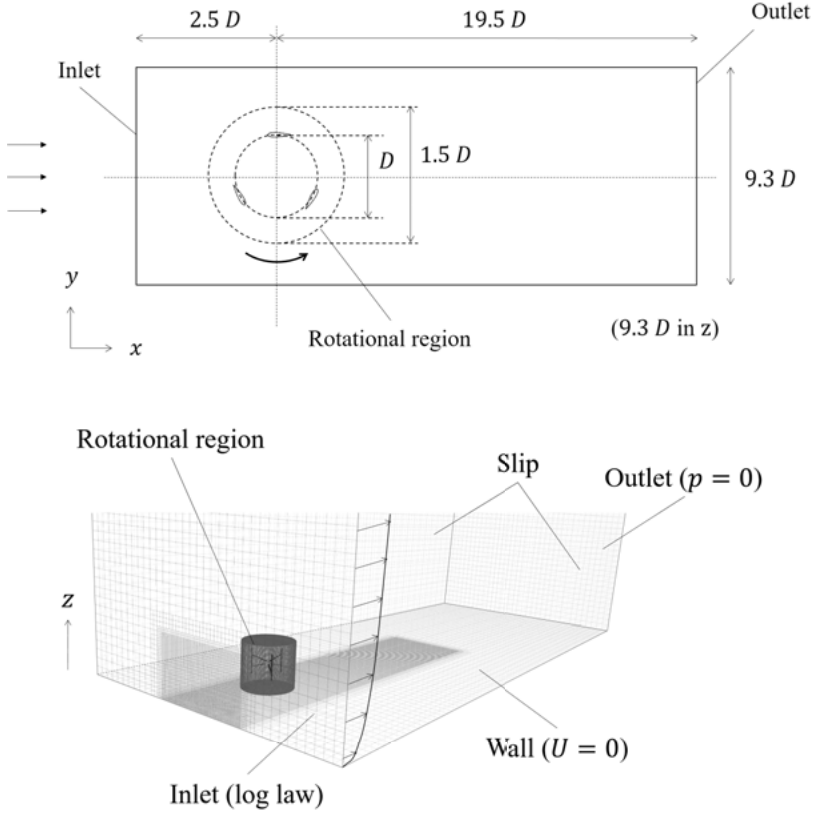


Figure 5.1. Computational domain (not to scale) and boundary conditions

model is known to perform well at predicting the adverse pressure gradients and the flow separation. Also, some studies [74, 75] recommend the SST-based models for the accurate simulation of Darrieus turbines among other commonly used turbulence models.

Time steps are adjusted so that the maximum Courant number is satisfied to be below 0.9. The average time step increment is around 8×10^{-6} sec, which approximately corresponds to time of rotating by azimuth angle of 0.0031° .

Figure 5.1 shows the computational domain and the boundary conditions. The domain consists of a rotational inner part and a stationary outer part. The rotational region is represented as the circular area of $1.5D$ diameter in the figure. The sizes of the entire domain in both the cross-stream and the vertical directions are $9.3D$. The sensitivity of the domain size to the simulation results is discussed in Paper III. The hub of the wind turbine is set to be positioned at the same height as in the real turbine.

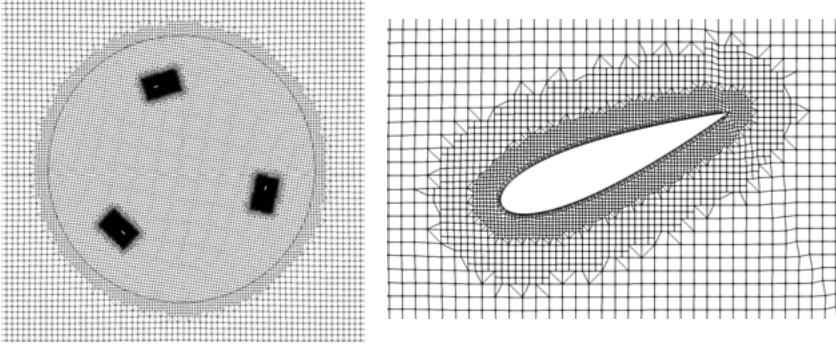


Figure 5.2. View of the mesh at the hub height in the rotational domain (left) and the area near the blade (right)

The inlet velocity is expressed by the log law. The log wind profile U_{log} varies with the height z and is defined as

$$U_{log} = \frac{U^*}{K} \ln \left(\frac{z - z_0}{z_0} \right) \quad (5.1)$$

where

$$U^* = \frac{KU_\infty}{\ln \left(\frac{z_{hub} + z_0}{z_0} \right)} \quad (5.2)$$

is the frictional velocity, $z_0 = 0.025$ m is the roughness length, $K = 0.41$ is the Kármán constant, and z_{hub} is the hub height. The turbulence kinetic energy k is set at the inlet so that the turbulence intensity $I = \sqrt{2k/3}/U_\infty$ is equivalent to around 0.1%. The pressure is assumed to be zero at the outlet boundary. The slip condition is applied at boundaries in the cross-stream and the vertical directions, except for the boundary on the bottom side at $z = 0$ where the wall boundary conditions are used to represent the ground.

Figure 5.2 shows the view of the discretized mesh at the hub height in the rotational inner domain and the area near the blade. The sliding interface between the rotating and the stationary zones can be seen as a circular line. The blunt edge of the blades is not modeled, so as to save the computational cost. The thickness of the first layer of the blade and strut surfaces is 1 mm, and the wall functions are applied at the boundaries of the surface. The mesh resolution meets the requirement for the wall functions that $y^+ < 300$.

Two simulation cases are studied: one contains the three blades and the other one additionally contains the six struts. The numbers of mesh cells for the cases without and with struts are 18 and 32 millions, respectively.

The steady-state flow is solved first to initialize the flow fields. More than 6 revolutions are computed using a coarse mesh to develop the wake for a few rotor-diameter distance, and then the last revolution is solved using the fine mesh described earlier.

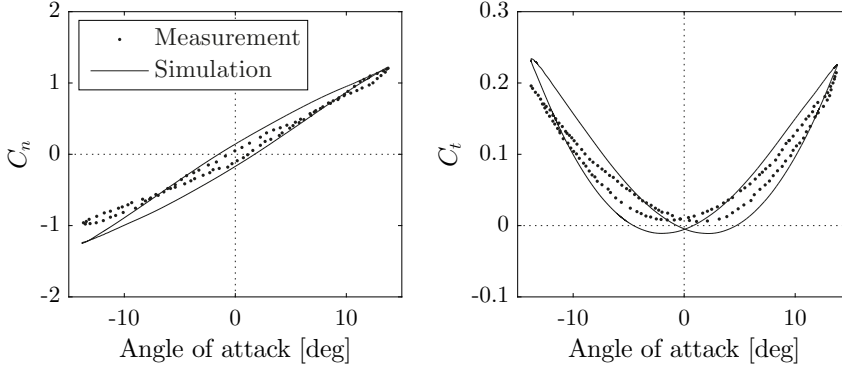


Figure 5.3. Normal and tangential force coefficients C_n and C_t of the pitching blade with the amplitude of the pitch angle of 13.8° (corresponding to the tip speed ratio of 4.19)

For the discretization of the convective terms, the second-order upwind Total Variation Diminishing (TVD) scheme is used to solve the last revolution. The diffusive terms are discretized by the central difference scheme. The bounded first-order implicit scheme is used for the time differencing.

5.2 Validation of numerical method

Single blade pitching motion

The numerical model is validated for the case of a sinusoidally pitching blade motion. This validation is made because the blades of VAWTs experience the sinusoidal variation of angle of attack during rotation, where the blade oscillation is dependent on the tip speed ratio.

The reference measurement was conducted by Angell et al. [76] for pitching motion of a NACA 0021 airfoil blade oscillating around the quarter chord position. The blade model has the chord length of 0.55 m and the span length of 1.61 m. The reduced frequency of the pitching oscillation is expressed as $k_{red} = c\Omega/2U_\infty$, and it is validated for the case when $k_{red} = 0.049$ and the amplitude of the pitching angle is 13.8° . This pitching angle corresponds to the blade motion at the tip speed ratio of 4.19. These test conditions, where the Reynolds number is 1.1×10^6 and the Mach number is 0.086, are in a reasonable range of the operational VAWT.

The measurement condition is simulated using the mesh which has the same relative cell size to chord length as the reference case. The normal and the tangential force coefficients C_n and C_t are compared against measurements as shown in Figure 5.3. C_n and C_t are defined as the normal and tangential forces normalized with $0.5\rho U_0^2 cL$ where ρ is the density of air, U_0 is the freestream

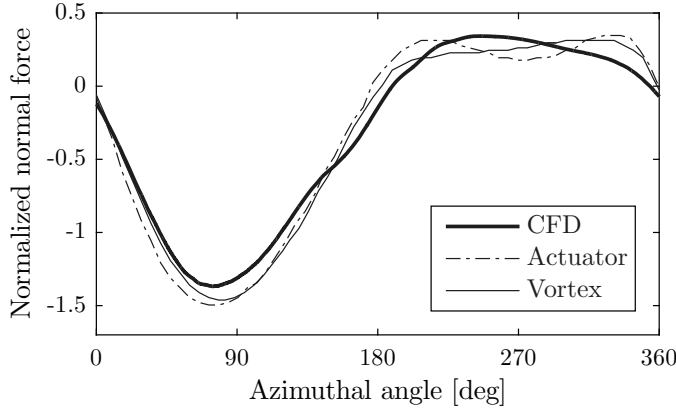


Figure 5.4. Comparison between the normalized normal force predicted by the CFD model of this study and the forces calculated using the actuator cylinder model and the free vortex model by Ferreira et al. [77] for the tip speed ratio of 4.5

velocity, and L is the span length. The comparison shows that the variation of the force is reproduced well for this tip speed ratio case.

Two-bladed VAWT

Another validation is made based on the case studied by Ferreira et al. [77] who validated several simulation models for a H-rotor VAWT with two blades of a NACA 0015 airfoil profile. The model of this study is validated by comparing the normal forces calculated using the actuator cylinder code developed by Madsen [78, 79] and the free vortex code developed by Murray and Barone [80]. It is tested for a tip speed ratio $\lambda = 4.5$ and the solidity $\sigma = N_{BC}/2R = 0.1$. This is the condition operated with the Reynolds number of the same order as that of the VAWT studied in this thesis. The ratio of the domain size to the rotor diameter and the resolution of the boundary layer mesh are kept equivalent to those of the reference case.

Figure 5.4 presents a comparison of the normalized normal forces expressed as $F_n/0.5\rho\lambda^2U_\infty^2c$ during one revolution. Although the CFD model slightly underestimates the force in the upwind side compared to the other two models, and there is a discrepancy of fluctuations seen in the downwind side, it ensures the sufficient accuracy for predicting normal forces.

5.3 Results and discussion

The performance of three different numerical models for reproducing the blade forces, namely, the full CFD model, the ALM, and the vortex model, is compared in order to examine how accurately each model is able to simulate the

strut effect. Three different tip speed ratios are considered, and the results are discussed in Section 5.3.1. In order to look more closely at flow features caused by the impact of struts, simulations are conducted using the CFD model for one high tip speed ratio case where the strut influence is especially pronounced, the results of which are presented in Section 5.3.2.

5.3.1 Comparison with different numerical methods

Table 5.1. List of the tip speed ratios λ studied in this section

λ	U_∞ [m/s]	ω [rpm]
2.6	6.6	49.9
3.4	6.4	64.8
4.2	5.3	65.0

Three tip speed ratios λ are tested in this section, and are listed in Table 5.1 with the corresponding freestream velocity U_∞ and rotational speed ω . The blade force of the VAWT is simulated for two cases with and without struts, using each numerical models.

Figure 5.5 and Figure 5.6 show the instantaneous velocity and vorticity fields in the vertical plane intersecting the turbine center for $\lambda = 3.4$ which are calculated by all three models for both cases with and without struts. To indicate the swept area, the plots include an illustration of the blades and struts located at $\theta = 90^\circ$ and 270° that are not actually in these positions in the simulation. They show the magnitude of the flow velocity normalized with U_∞ and the y component of the non-dimensionalized vorticity which is calculated by $(\nabla \times \mathbf{U}) \cdot \mathbf{c} / U_\infty$. Figure 5.7 and Figure 5.8 show the velocity and vorticity fields in the horizontal plane at $z/D = 0.97$ that is in the middle between the hub height and the upper strut attachment point. The velocity and vorticity illustrated are the values in y and z directions, respectively. It is noted that the CFD and the ALM consider the wind shear, while the vortex does not.

It can be seen from all plots in Figure 5.5 and Figure 5.6 that vortices are shed from the blade tips and travel downstream. Both the CFD and the vortex models represent the strut influence clearly in the rotor and the wake regions where the velocity is less uniform and stronger vortices are observed for the case with struts. The vortex model especially reproduces the complex structure of vortices. The pictures from the ALM-SK and the ALM-XF do not show so noticeable influence of the struts as for the CFD and vortex models.

The above findings are also confirmed from Figure 5.7 and Figure 5.8, i.e. the CFD and vortex models show more pronounced differences between two cases than the ALM. The pictures from the CFD and vortex models clearly show vortices generated from the blades and the struts which can affect the

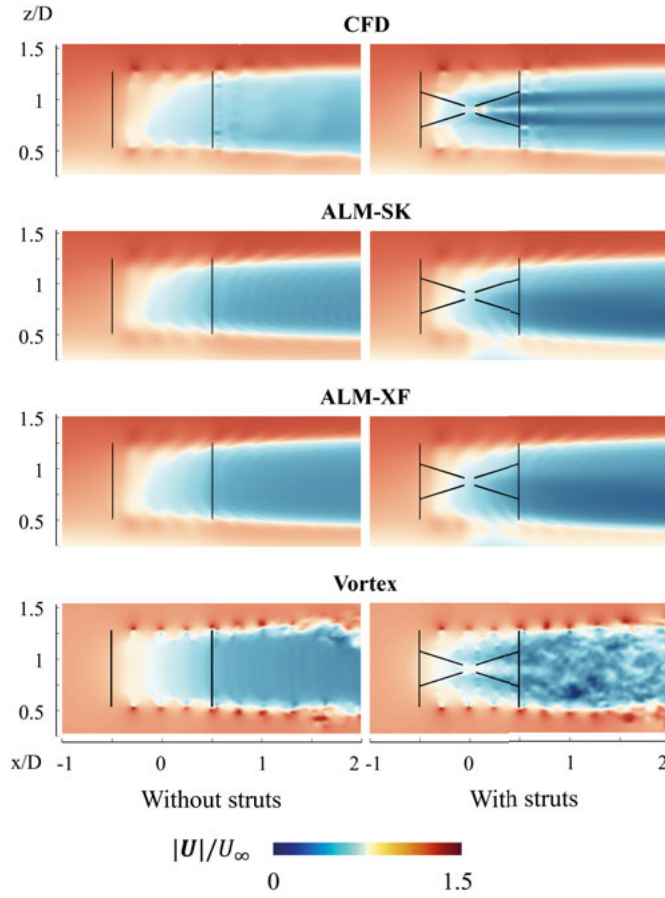


Figure 5.5. Instantaneous magnitude of the velocity in the vertical plane intersecting the center simulated by the three models for the cases without and with struts ($\lambda = 3.4$)

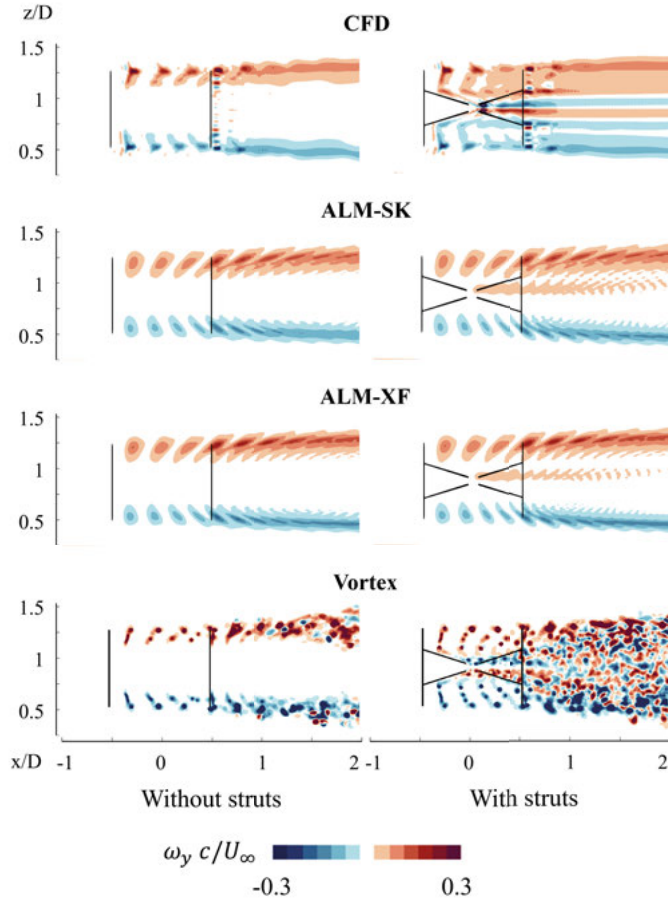


Figure 5.6. Instantaneous vorticity in y direction in the vertical plane intersecting the center simulated by the three models for the cases without and with struts ($\lambda = 3.4$)

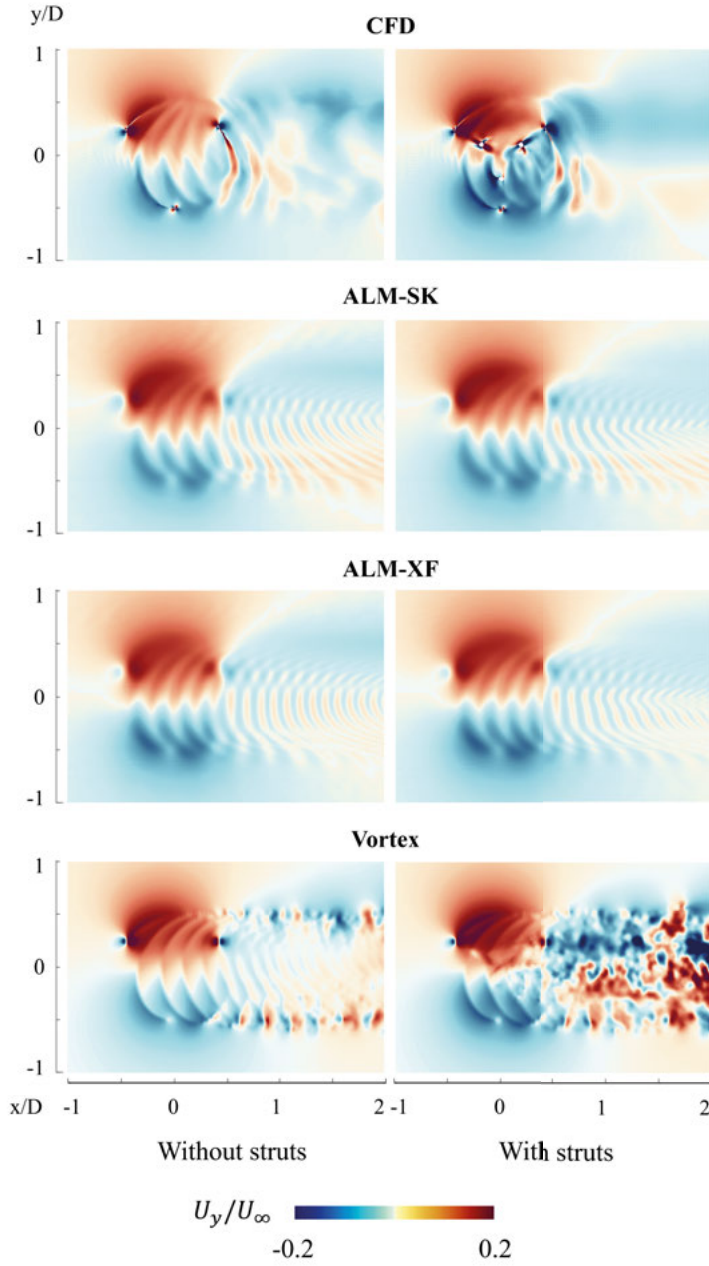


Figure 5.7. Instantaneous velocity in y direction in the horizontal plane at $z/D = 0.97$ simulated by the three models for the cases without and with struts ($\lambda = 3.4$)

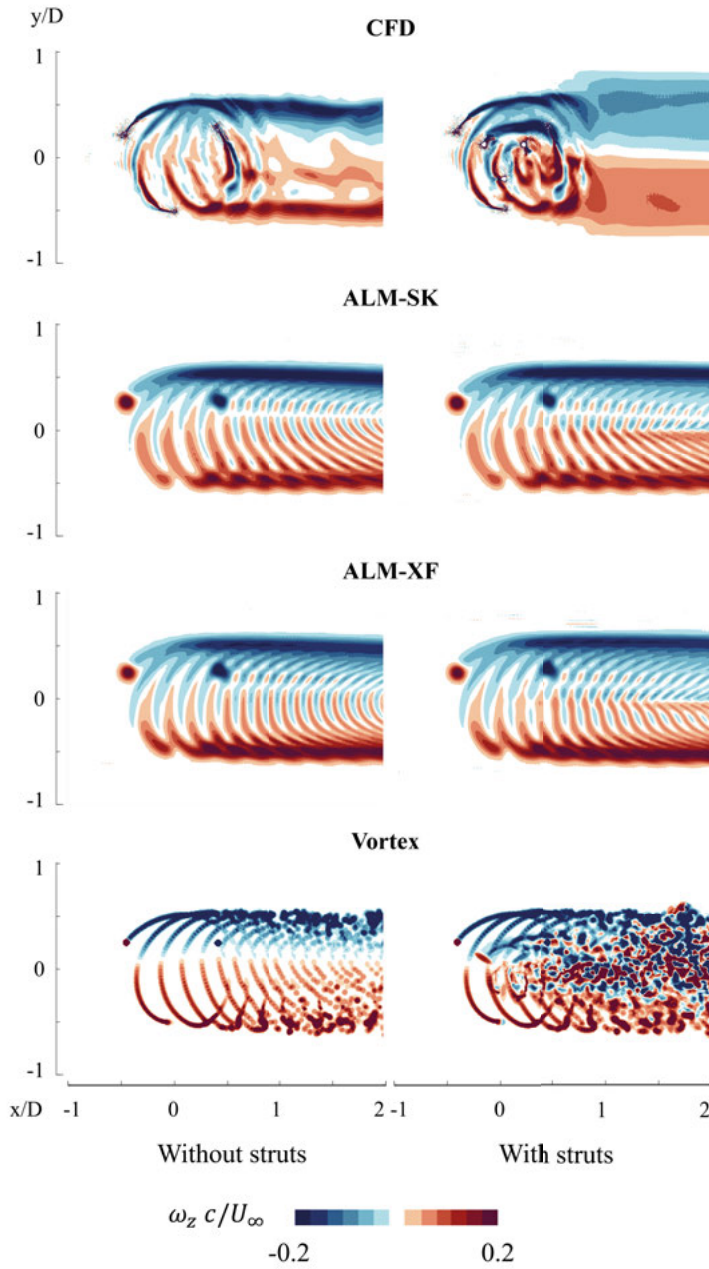


Figure 5.8. Instantaneous vorticity in z direction in the horizontal plane at $z/D = 0.97$ simulated by the three models for the cases without and with struts ($\lambda = 3.4$)

blades rotating in the downwind side. Both the ALM-SK and ALM-XF produce strong vortices convected downstream maintaining their pattern, but there is no remarkable differences observed on account of the struts.

Figure 5.9 shows the comparison of normal forces over one revolution calculated using the three models for two cases with and without struts at all three tip speed ratios, $\lambda = 2.6, 3.4$, and 4.2 . The plots also include the forces measured by Dyachuk et al. [81, 82], and the measurement data shown here is the average from around 8 revolutions.

The results show that two curves with and without struts cases are quite similar for each of the models at all tip speed ratios, which indicates that none of the models represent any significant impact of struts on the total normal force. All three models overpredict the amplitude in the upwind side compared to the measurement, especially for λ of 2.6 and 3.4 . There is a drop of the measured force at around 270° for λ of 3.4 and 4.2 , which is also not present in the prediction.

If compared among the three models, the discrepancies of the force amplitude are more pronounced for smaller tip speed ratios. When λ is 2.6 , the force predicted by the CFD model fluctuates at $\theta = 220^\circ$ for both cases with and without struts. The dynamic stall phenomenon, which is likely to occur at low tip speed ratio, can be observed in the flow field around airfoil simulated by the CFD model at this azimuth angle. Neither the ALM nor the vortex model include this behavior of the vortex released from the leading edge in the dynamic stall model. On the contrary, the amplitude is quite close among all the predicted curves for the high tip speed ratio $\lambda = 4.2$ where the dynamic stall is less expected to occur.

Figure 5.10 shows the comparison of the distribution of the normal force per unit length F_n^* when the blade is located at $\theta = 90^\circ$ and 270° for all three tip speed ratios. The values of F_n^* at $\theta = 90^\circ$ and 270° are plotted on the left and right sides within each plot.

When the struts are not considered, the amplitude of the forces predicted by the three models is close at all the tip speed ratios with the exception of the prediction by the ALM-XF at $\lambda = 2.6$. The ALM-XF overpredicts at both azimuth angles, as the flow predicted is not properly stalled. The ALM-SK and the vortex models use the same force model and therefore are close to each other.

Although there is no significant influence of struts in the total forces as shown in Figure 5.9, Figure 5.10 indicates that the struts strongly affect the force distribution especially in the downwind side, $\theta = 270^\circ$. It is obvious at λ of 3.4 and 4.2 that the CFD and vortex models have the curves of irregular profile shapes when the struts are considered. At $\lambda = 2.6$, these differences can only be recognized clearly in the CFD model. The influence of struts is not equally distinct in the ALM at all tip speed ratios. This is because the struts are

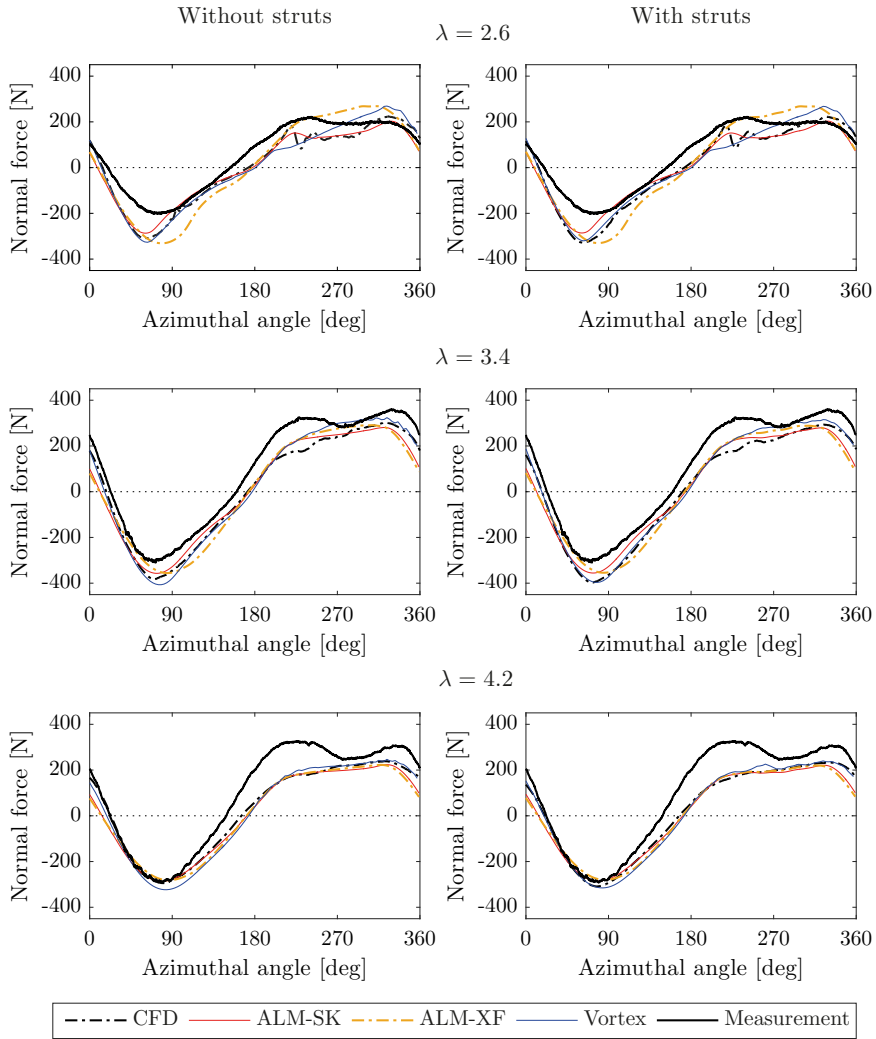


Figure 5.9. Normal forces during one revolution simulated using the CFD model, the ALM, and the vortex model compared with measured forces for $\lambda = 2.6$ (top), 3.4 (middle), and 4.2 (bottom). Plots on the left and right sides show the results computed without and with struts.

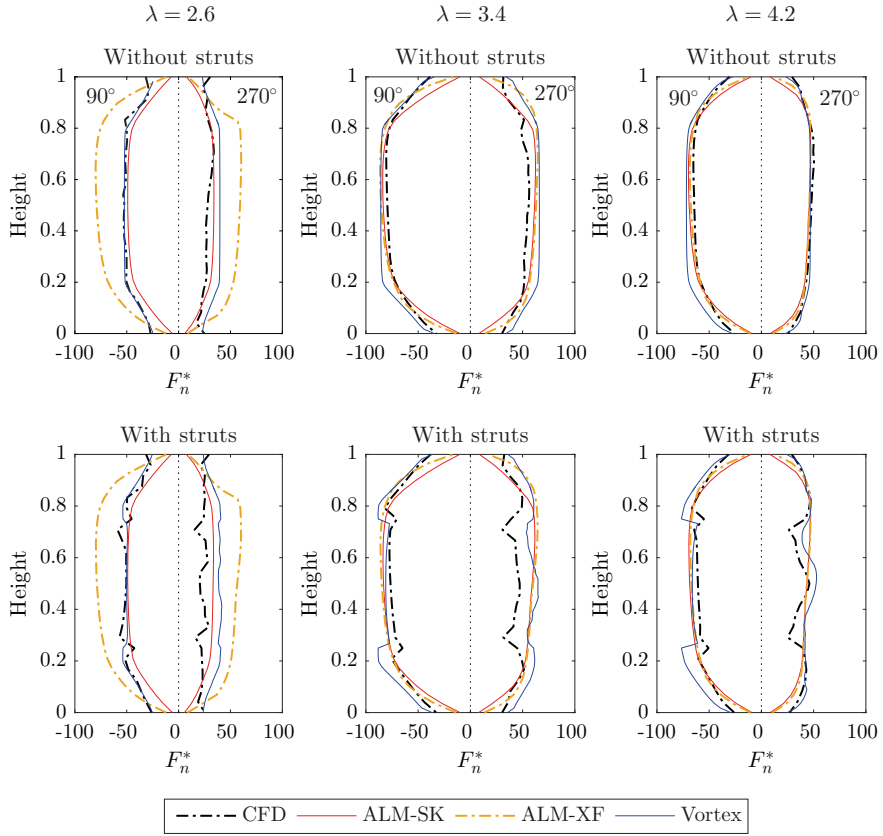


Figure 5.10. Comparison of the normal force distribution along blade at $\theta = 90^\circ$ and 270° predicted using the CFD model, the ALM, and the vortex model for $\lambda = 2.6$ (left), 3.4 (middle), and 4.2 (right). Forces simulated without and with struts are presented in the top and bottom rows

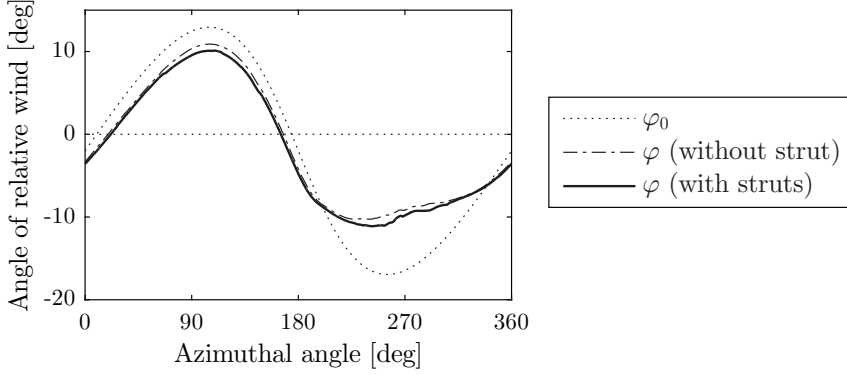


Figure 5.11. Angle of relative wind ignoring the induced velocity φ_0 and the angle of relative wind φ for cases with and without struts at the middle height of the blade

considered as independent wings with their own tip vortex at the end, while the other models consider them as a coupled system.

5.3.2 Case study for high tip speed ratio

One case simulated by the CFD model for high tip speed ratio is presented in this section, to further investigate the influence of the presence of struts on the aerodynamics of the VAWT. The freestream velocity and the rotational speed considered in this section are $U_\infty = 6.4$ m/s and $\omega = 77.1$ rpm, which leads to the tip speed ratio $\lambda = 4.1$.

The induced velocity \mathbf{U}_{wind} is estimated by sampling the flow velocity along the circular path of the blades, then the relative velocity \mathbf{U}_{rel} is calculated using Equation (2.16). It can be found from the relative velocity that the average of the local Reynolds number based on the chord length during revolution is around 4×10^5 .

The angle of relative wind φ is calculated from \mathbf{U}_{rel} using Equation (2.17). Figure 5.11 shows φ at the middle height of the blade $0.5H$ for the two cases when the struts are and are not considered. Neither case represents significant differences of φ , and it varies within the range of ± 11 degrees approximately. The angle when the wind is undisturbed, that is φ_0 , is also depicted. The large reduction of φ from φ_0 can be noticed in the downwind side.

Figure 5.12 shows the vortex structure around the rotor with the blades located at $\theta = 15^\circ$, 135° , and 255° . The Q-criterion is used to visualize the vortex formation. It calculates the second invariant of the velocity gradient tensor, which is expressed as $Q = 0.5(\Omega_{ij}\Omega_{ij} - S_{ij}S_{ij})$ where $\Omega_{ij} = 0.5(\partial u_i/\partial x_j - \partial u_j/\partial x_i)$ is the vorticity tensor and $S_{ij} = 0.5(\partial u_i/\partial x_j + \partial u_j/\partial x_i)$ is the rate-of-strain tensor. Figure 5.12 represents the isocontour for $Q = 6$. It can be observed in both cases that tip vortices are released from top and bottom

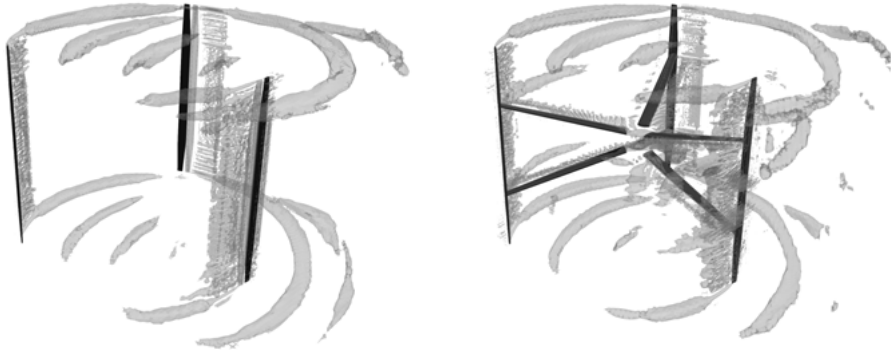


Figure 5.12. Vortex structure represented using isocontour of $Q = 6$ for the cases without struts (left) and with struts (right)

sides and convected downstream. Additionally, vortices are generated from the height of the attachment points when the struts are included in the simulation.

Figure 5.13 shows the normalized pressure distribution for the upper part of the blade surface located at azimuth angles from $\theta = 220^\circ$ to 300° , seen from the outside of rotation. The influence of the presence of the struts can be seen at the height of the attachment point. Fluctuations can also be recognized more clearly at around the middle of the blade for the case with struts, especially at 240° and 260° . The pressure distribution and contour plot of the vorticity in Paper III imply that the flow is largely separated and that the vortices are generated at the height of the strut attachment when they are considered in the simulation.

Figure 5.14 shows the contour plots of the normal force distribution along the blade per unit length F_n^* during one revolution. Figure 5.15 shows the force distribution at selected azimuth angles, $\theta = 90^\circ, 180^\circ, 225^\circ, 270^\circ$, and 315° . The blade surface is split into 25 segments along the height and the force of each segment is monitored during simulations.

There is a clear difference in the contour plots at the normalized height of the strut attachment 0.27 and 0.73, and the struts strongly affect the forces not only in the downwind, but also in the upwind side of rotation. It is easily recognizable also in Figure 5.15 that the sudden drop of the forces appears at the height of attachment. Figure 5.14 also illustrates the influence of struts not only at the attachment height but also over the large area of the blade height where the wake generated from the struts can interact, i.e. the projection area of the entire span section of the struts to the blade. The force is relatively high along the blade at around $\theta = 210^\circ$ and starts to decrease toward 270° then increases again.

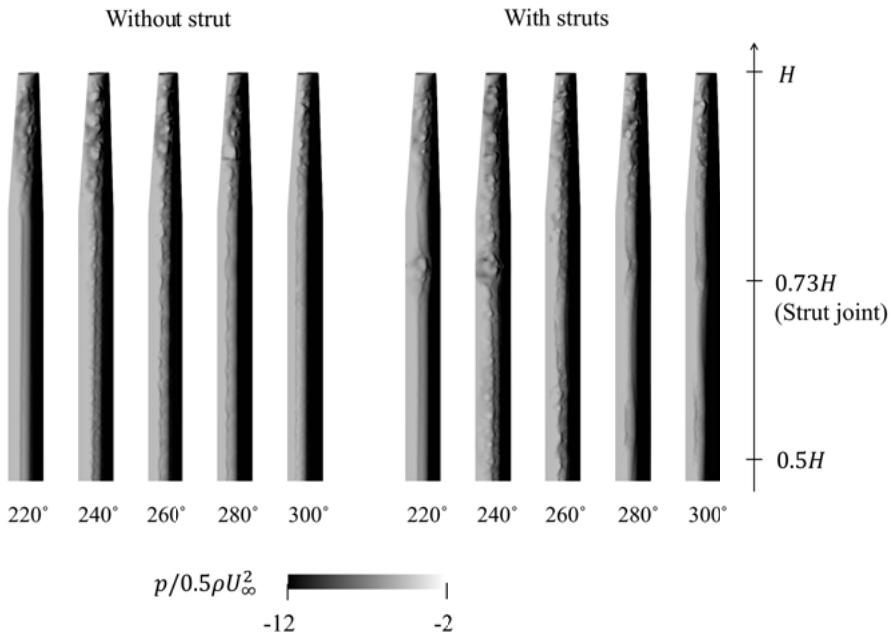


Figure 5.13. Pressure distribution of the blade surface on the outer side of rotation at every 20° azimuth angle from $\theta = 220^\circ$ to 300° for the cases without struts (left) and with struts (right)

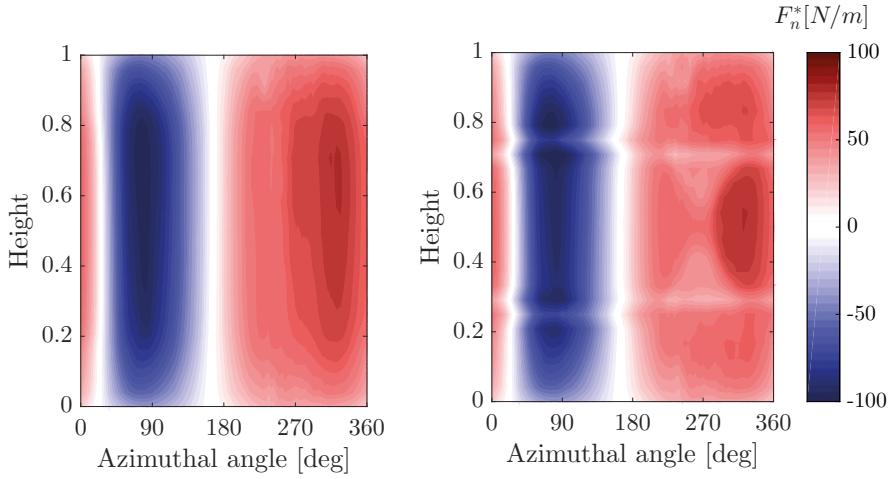


Figure 5.14. Contour plot of the normal force distribution of the blade for the cases without struts (left) and with struts (right)

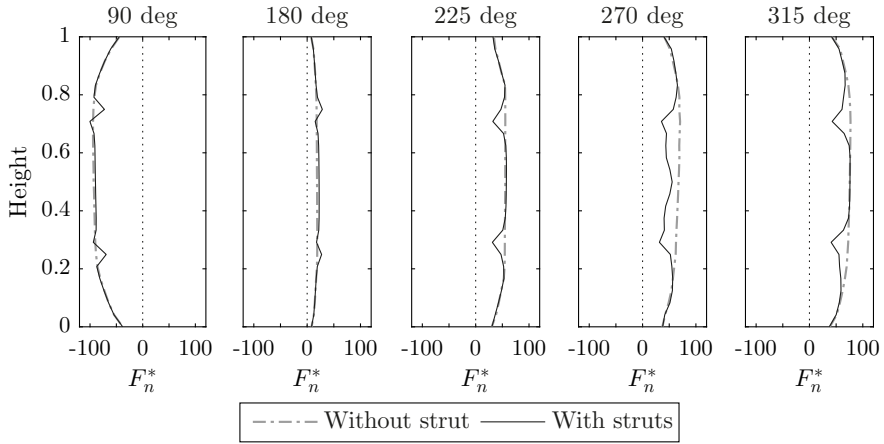


Figure 5.15. Comparison of the normal force distribution along the blade at selected azimuth angles

6. Aeroacoustic studies for vertical axis wind turbine

This chapter summarizes the studies for the prediction of the VAWT noise. The approach for LES and the acoustic measurement method are briefly described first. The noise is predicted for the turbine operating at high tip speed ratio, and the obtained sound pressure is validated against the measurement data. The characteristics of the flow behavior are analyzed from the simulation results which are related to the sound sources dominating for this VAWT.

6.1 Numerical method

An incompressible flow is solved using LES to calculate the sound sources around the VAWT. The WALE (wall adapting local eddy-viscosity) turbulence model [83] is used as a SGS model.

The first and second-order schemes are used for the temporal and spatial discretization, respectively. The sizes of the computational domain are 19D and 9D in the cross-stream and the vertical directions. All the boundary conditions are specified in the same manner as described in Section 5.1, except for the boundaries on the blade and strut surfaces where the flow is solved with no approximation of wall boundaries.

All three blades and six struts are modeled in the simulation, but fine refinement of mesh is applied only for the surfaces of a single blade and two struts attached to it, in order to reduce computational cost. The thickness of the first layer of these surfaces is less than 0.03 mm, which results in the values of y^+ less than 3. The blunt edge of the blade is the size in the order of a millimeter and is ignored in the mesh, while the blunt edge of the struts, being a few centimeters thick, is taken into consideration. Other components, such as a tower, are not included, assuming that the dominant noise source is generated from the blades and struts. This results in a total number of 50 million mesh cells. See Paper V for other details of the numerical setup. The validation for the noise prediction method using the present mesh is performed for a single static blade case; the results are presented in Paper V as well.

6.2 Acoustic measurement

The measurements were performed between 14:20 and 14:50 on September 9th, 2020. The wind came approximately from the South. The temperature



Figure 6.1. Microphone

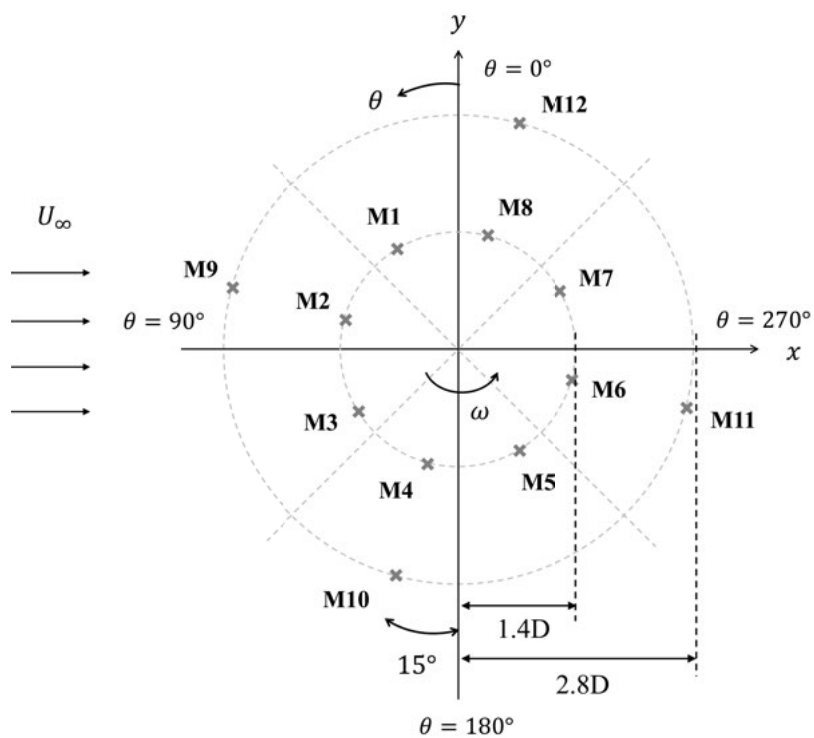


Figure 6.2. Locations of sound observation

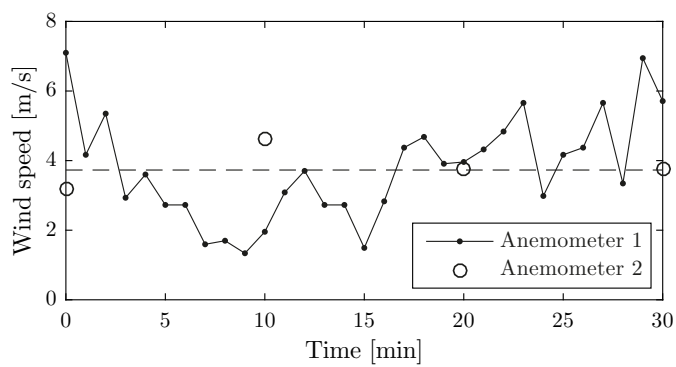


Figure 6.3. Wind speed at hub height recorded by two different anemometers during the entire measurement time with the average value used in simulation represented by the dashed line

was around 17 °C. The sound was measured with a Class 1 Sound Level Meter (Brüel & Kjær 2270) and calibrated prior to each new measurement position using a Larson-Davies CAL200 calibrator at 94 dB. The microphone was mounted horizontally at 1.2 m height as shown in Figure 6.1 and directed towards the wind turbine. Reported numbers are one minute equivalent sound levels from each position, and this time period approximately corresponds to the duration of 50 revolutions of the rotor. It is considered that the background sound was originating from a road at 1 km distance to the East of the wind turbine site.

Figure 6.2 shows the locations where the sound was recorded. The sound was recorded for 8 and 4 azimuthal directions at the radial distances of $1.4D$ and $2.8D$, and these locations are arranged at every 45° and 90° with all positions shifted clockwise by 15° , respectively.

Figure 6.3 displays the variation of wind speed during the total recording time measured by two different anemometers. One anemometer measures the instantaneous wind at hub height every minute which is shown with a line. The other one measures the 10-minute average wind at 4 meter height; these values are corrected to the wind speed at hub height using Equation (5.1) and are shown with markers. The mean values for the freestream velocity U_∞ and the rotational speed ω during the recording time are 3.7 m/s and 49.1 rpm, which results in the tip speed ratio of 4.5. The dashed line in Figure 6.3 represents this mean value of wind speed that is used in the simulation.

6.3 Results and discussion

The predicted SPL is validated by comparing with measurement data. Figure 6.4 and Figure 6.5 show the A-weighted one-third octave band spectra of the SPL with reference p_{ref} observed at radial distances of $1.4D$ and $2.8D$ for 8 and 4 different directions, respectively. The measured SPL at frequencies up to 100 Hz can be considered to originate from the noise of the road traffic.

The measurement data have broadband characteristics centered at around 630 Hz or 800 Hz. The maximum SPL in Figure 6.4 is generally underestimated by a few decibels, except for those at the locations of M3 and M7 which have differences by almost 10 dB. The possible reason for these large discrepancies is that the model does not simulate the actual wind conditions. The wind speed changed rapidly during the recording period as shown in Figure 6.3. Thus, it can be considered that the tip speed ratio intermittently became quite low, assuming that the rotational speed was constant. Dynamic stall is likely to occur at low tip speed ratio, which in turn generates large noise induced separation.

The discrepancies become even larger at a longer distance of $2.8D$ as shown in Figure 6.5, and these differences can be considered to be caused by neglecting the ground effect. The observer receives both the direct sound wave and

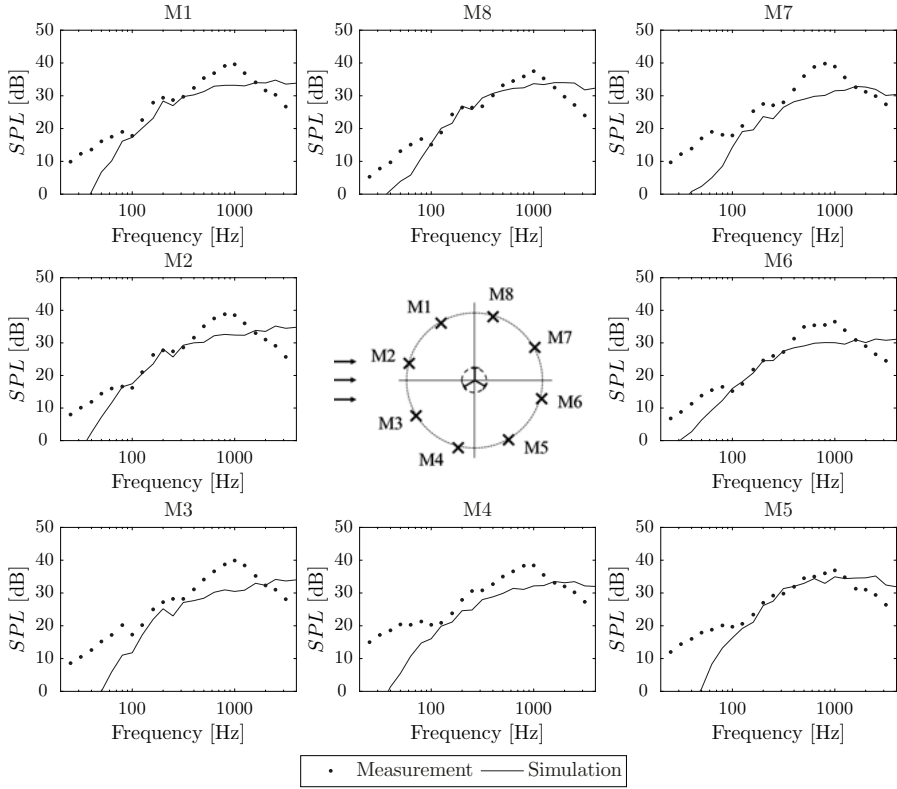


Figure 6.4. 1/3 octave band spectra of the measured and predicted sound pressure level observed at radial distance of $1.4D$ from the center of rotation with reference P_{ref}

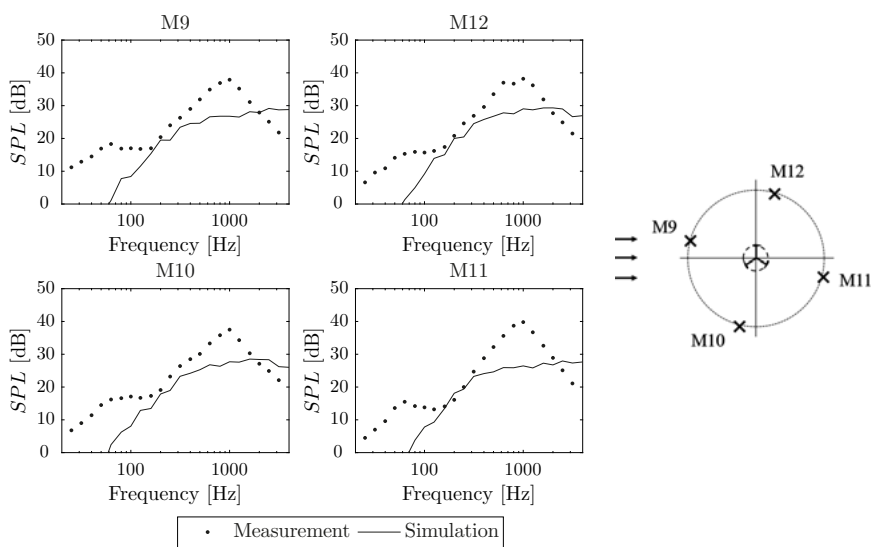


Figure 6.5. 1/3 octave band spectra of the measured and predicted sound pressure level observed at radial distance of $2.8D$ from the center of rotation with reference P_{ref}

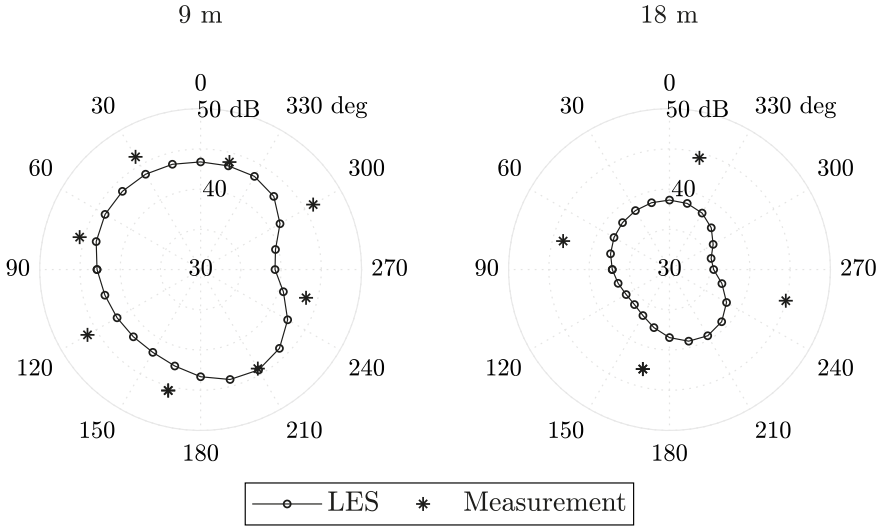


Figure 6.6. Directivity of the predicted and measured overall SPL at radial distances of $1.4D$ (left) and $2.8D$ (right)

the wave reflected from the ground, but only the direct sound is considered in the simulation. The ground effect is expected to be more significant at greater distance, and if this is the case, care has to be taken when simulating the noise received at long distance.

Figure 6.6 shows the directivity pattern of the predicted and measured overall SPL at radial distances of $1.4D$ and $2.8D$. They are calculated by summing up the SPL of the frequency bands from 25 Hz to 3100 Hz. There is no significant dependence of directivity in the measurements, while the prediction indicates strong directivity that the overall SPL is higher in the upwind than in the downwind side for both radial distance cases.

The decay of the predicted overall SPL by doubling the distance is consistent with the theoretical values for the attenuation of the sound by the distance from the sound source. The decay presented in Figure 6.6 for each of the 24 observation directions falls within the range of between 3.7 dB and 5.9 dB. These numbers are less than the theoretical decay for spherical spreading per doubling of distance that is 6 dB, but larger than the decay for cylindrical spreading that is 3 dB.

The sound emitted from the blade is more dominant in the total noise than the sound from the struts. Figure 6.7 shows the overall SPL radiated from only a single blade, only two struts, and both of them. The presented values are the sound observed at radial distances of $1.4D$ for different azimuth angles. It is obvious that the overall SPL from the blade is much larger than the SPL from struts at all azimuth directions.

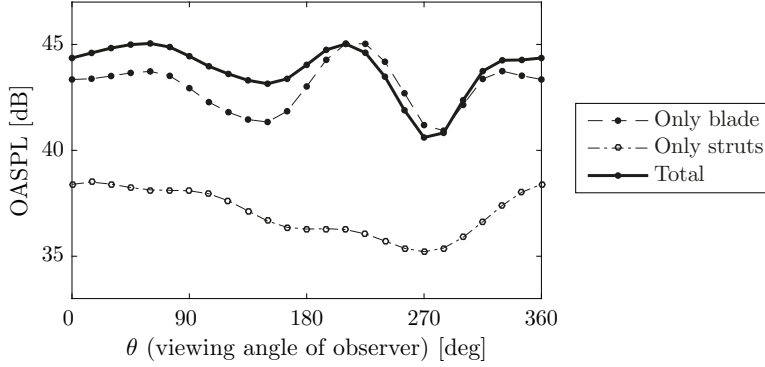


Figure 6.7. Overall SPL radiated from only a single blade, only two struts, and both of them for observation locations around different azimuthal directions at radial distances of $1.4D$

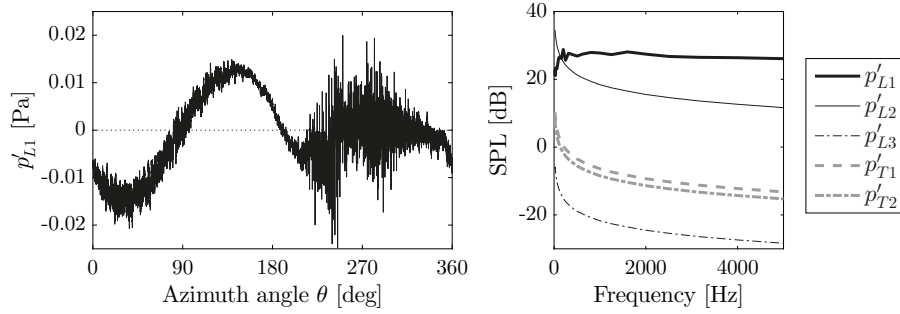


Figure 6.8. Time history of the term related to the pressure derivative in the loading noise during one revolution (left) and spectra of the SPL attributed to each term in the loading and thickness noise (right). The data presented are the sound pressure observed at $\theta = 90^\circ$ at distance $1.4D$ radiated from a single blade and two struts

The first term in the loading noise expressed by Equation (2.9) includes the variable of the time derivative of pressure \dot{p} , and the time history of this term p'_{L1} during one revolution is shown in the left plot in Figure 6.8. The spectra of the SPL attributed to three and two terms of each integral in the loading and thickness noise represented in Equation (2.9) and Equation (2.8), denoted by p'_{L1} , p'_{L2} , p'_{L3} , p'_{T1} , and p'_{T2} , are shown in the right plot in Figure 6.8. The presented data correspond to the sound pressure observed at $\theta = 90^\circ$ at distance $1.4D$ radiated only from a single blade and two struts.

It can be seen from the left plot that p'_{L1} fluctuates more largely when the blade travels in the downwind than in the upwind side. The right plot indicates that the terms of the loading noise are more dominant than those of the thickness noise, and especially the contribution of the term p'_{L1} is highest in almost all frequency range. Some studies [40, 41, 31] found that the thickness noise is the dominant noise source for VAWTs of smaller scale. The loading

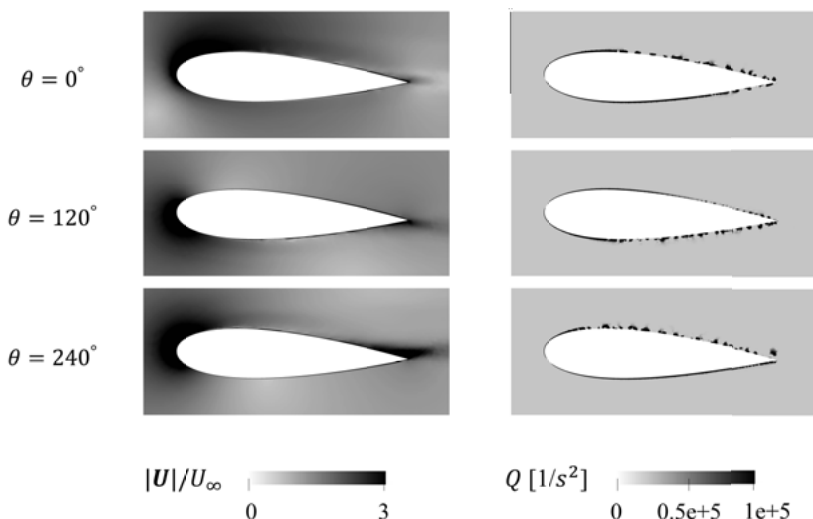


Figure 6.9. Velocity field (left) and vortex structure (right) around the blade at the middle height located at $\theta = 0^\circ$, 120° , and 240°

noise plays a more important role for this VAWT, as the rotational frequency is much lower and is less relevant to the audible range.

Figure 6.9 shows the velocity field and vortex structure around the blade at the middle height located at azimuth angles $\theta = 0^\circ$, 120° , and 240° . The upper side of the airfoil in the pictures corresponds to the outer side of the rotation. The magnitude of the velocity is normalized with U_∞ . The vortex formation is visualized using the Q-criterion in the same manner as in Section 5.3.2. Since the tip speed ratio is high, the flow mostly remains attached and no significant large vortex is shed in the wake behind the blade. However, the separation of the boundary layer can be seen in the vicinity of the trailing edge, especially at $\theta = 240^\circ$. It can also be observed from the pictures of the vortex structure that the transition of the boundary layer to turbulence occurs at the first half of the chord, and that small vortices cover a large area of the airfoil surface on the suction side. The vortex shedding is present on the surface close to the trailing edge of the pressure side at 0° and 120° , but not at 240° .

A swishing sound was heard clearly during the measurement; the turbine apparently emits this loud sound when the blade passes at a certain azimuth location during revolution. In order to estimate the azimuth position where the sound is strongly generated, the instantaneous overall SPL during revolution is calculated as shown in Figure 6.10. The presented data correspond to the sound radiated from a single blade and two struts observed at radial distances of $1.4D$ and $2.8D$ from 4 different azimuth angles, $\theta = 0^\circ$, 90° , 180° , and 270° . In the calculation, the data series of the sound pressure during the time period for the blade to rotate by 30 degrees is extracted, and is filtered to

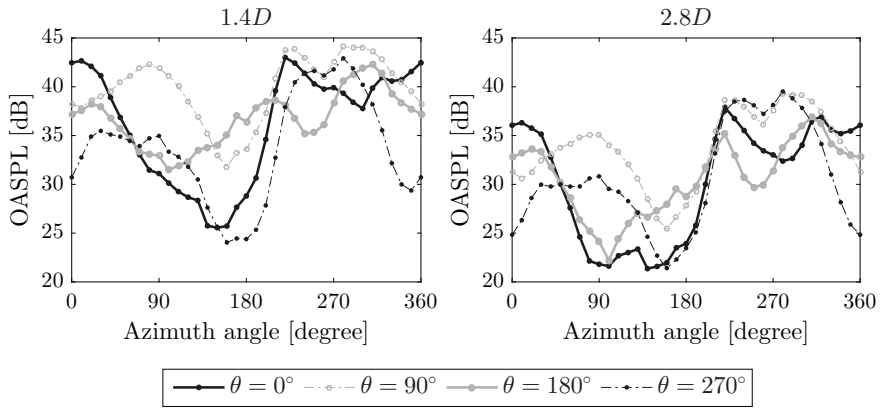


Figure 6.10. Instantaneous overall SPL during revolution observed from 4 different azimuth angles, $\theta = 0^\circ, 90^\circ, 180^\circ$, and 270° at radial distances of $1.4D$ (left) and $2.8D$ (right)

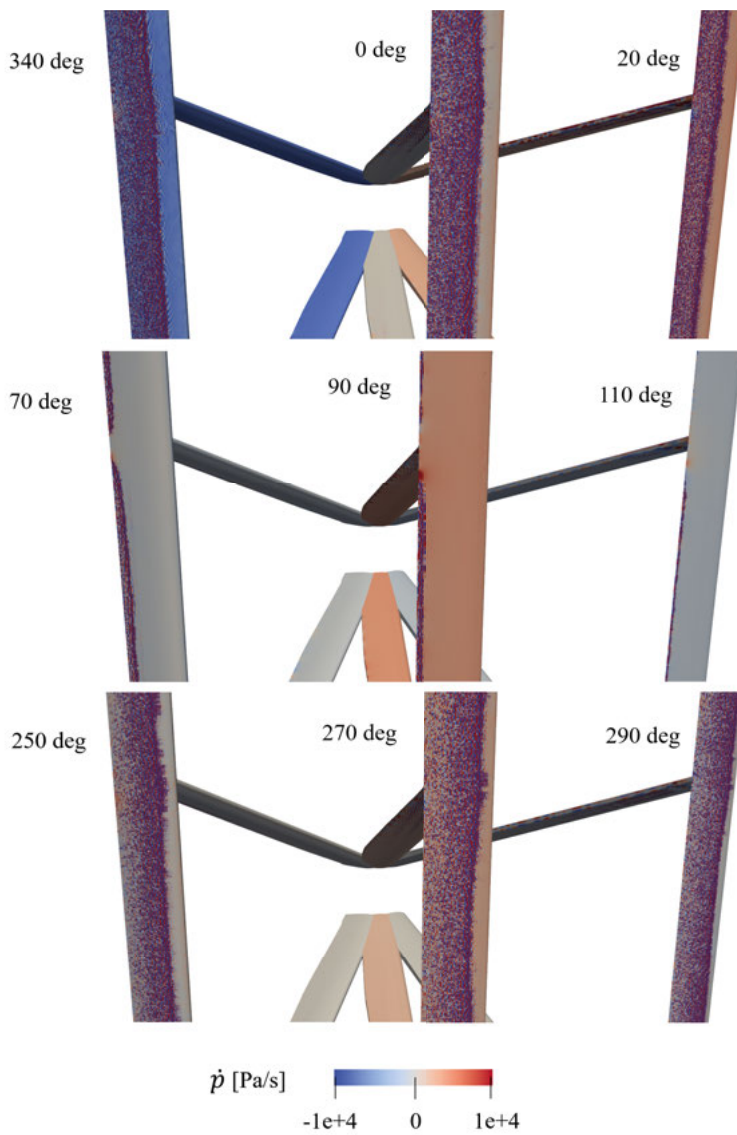


Figure 6.11. Time derivative of surface pressure seen from the outside of the rotor

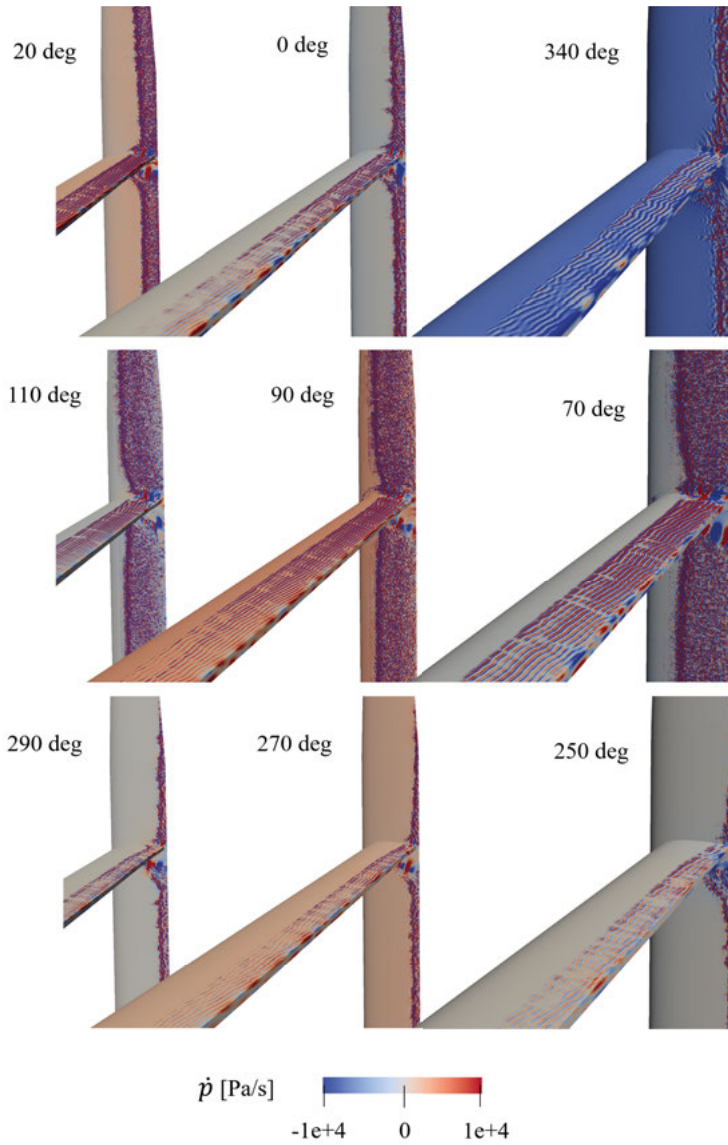


Figure 6.12. Time derivative of surface pressure seen from the inside of the rotor

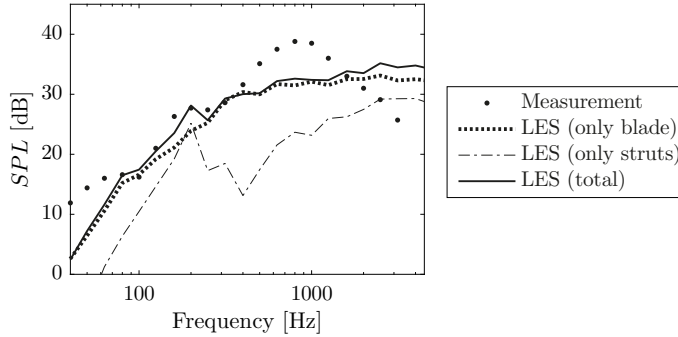


Figure 6.13. 1/3 octave band spectra of the SPL observed at M2 calculated radiated from only the blades, only the struts, and both of them

obtain the spectrum after the hanning window is applied. Then, the overall SPL is obtained by summing up the SPL in all bands. It can be seen from this figure that the received sound is likely to be louder when the blade passes in the downwind than in the upwind side. This is probably because the blades moving in the downwind suffer from the wake created by the blades and struts in the upwind, and the interaction of the wake contributes to generate large sound sources.

Figure 6.11 and Figure 6.12 show the time derivative of pressure \dot{p} on the surface seen from the outside and inside of the rotor when the blade and struts are located at several different azimuth angles. Both figures indicate that intensive fluctuation of \dot{p} is concentrated around the trailing edge at all azimuth angles presented. Small fluctuations can be seen over a large area of the surface on the suction side of the blade, and the fluctuations are present on the pressure side in the area close to the trailing edge as well. It can be assumed that these small fluctuations at the surface attribute to the source of the trailing edge noise as they convect past the trailing edge of the airfoil. Figure 6.12 also indicates that the wavy pattern occurs on the strut surface, while the pressure fluctuates more randomly on the blade surface.

The inflow turbulence noise is not properly simulated, but it could be another important sound source for this turbine. Inflow turbulence noise is generated primarily by the passage of eddies from the atmospheric turbulence in the approach flow over the leading edge of the airfoil [84] where local pressure fluctuations are induced. However, no significant pressure fluctuation can be observed at the leading edge in Figure 6.11 and Figure 6.12. One of the reasons why the SPL presented in Figure 6.4 and Figure 6.5 is underpredicted could be that the simulation does not include turbulence in the freestream wind and thus is not able to properly reproduce the inflow turbulence noise.

It can be considered that the second small peak observed in the measured spectra in Figure 6.4 is caused by the sound source from the strut surface. Fig-

ure 6.13 shows the spectra of the SPL observed at the location of M2 radiated from only the blades, only the struts, and both of them. The peak at 200 Hz is highly dominant in the spectrum which considers only the struts, but does not appear when they are not included.

In order to illustrate the vortex structure around the trailing edge of the strut, the pictures to the left in Figure 6.14 show the isocontour for $Q = 60$ when the strut is located at $\theta = 90^\circ$ and 270° . The pictures to the right show the time derivative of surface pressure \dot{p} on the blade surface around the strut attachment location. From the pictures to the left, more complex vortex structure can be seen around the strut joint at $\theta = 90^\circ$ than at 270° . It can also be observed from the pictures to the right that the joint causes fluctuations in a larger area on the blade surface around the strut connection at $\theta = 90^\circ$. Figure 6.15 represents the contour plot of Q for the upper strut at $\theta = 270^\circ$ at the plane sliced perpendicular to the span at 93% of rotor radius. This plot indicates that the vortices start to be created in the middle of the chord on both sides and are released while interacting with the blunt trailing edge. In the wake of the blade, on the other hand, no vortex shedding can be observed. The local flow around the struts is different from that of the blades, as the struts have separation due to the blunt trailing edge and the tip speed ratio is low at small radius. This flow characteristics around the struts can be considered to generate the tonal noise observed at 200 Hz.

The characteristic frequency in the sound spectrum significantly varies during revolution, depending on the azimuthal position of the blade and struts. Figure 6.16 shows the spectra of the instantaneous SPL observed at the radial distance of $1.4D$ from 4 different azimuth angles, $\theta = 0^\circ, 90^\circ, 180^\circ$, and 270° . The presented sound is that radiated from a single blade (left) and two struts (right) when they pass at 90° and 270° . The dominant frequency of sound from the blade is observed at 800 Hz from all observation points when it passes at 270° , but the spectra have the highest peak at 400 Hz when it travels at 90° . It can be seen from all observation points that the peak at 200 Hz is prominent in the spectra of struts passing at 90° , but it is not clearly observed when the struts move at 270° .

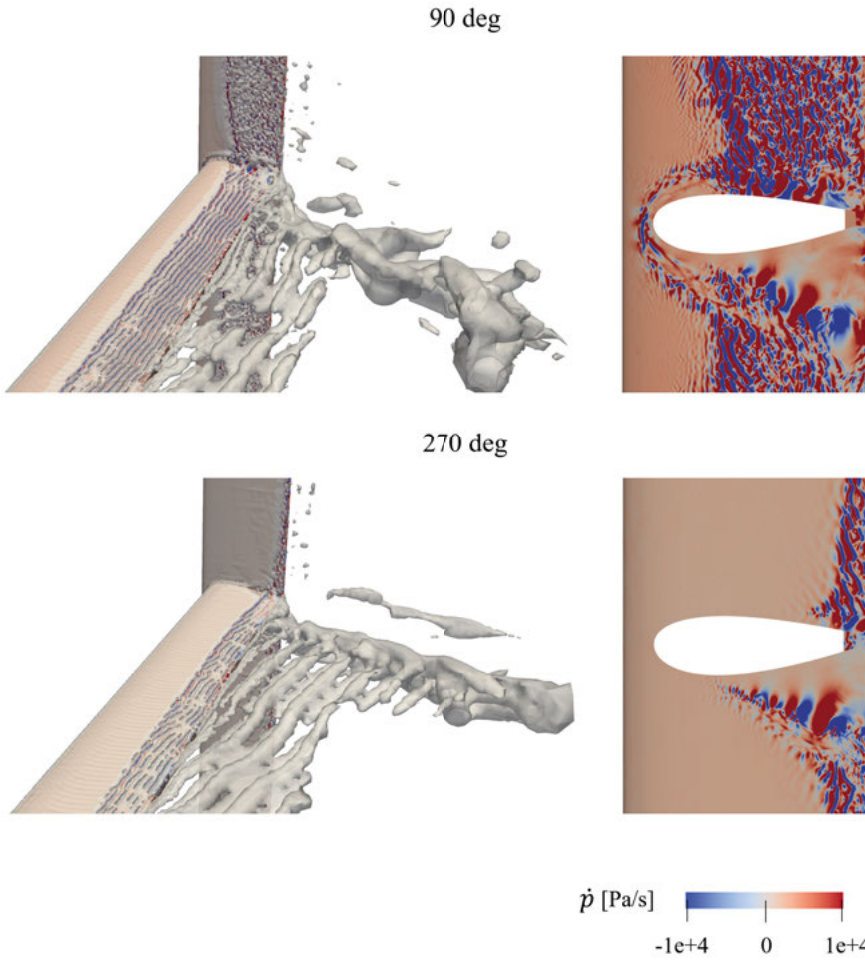


Figure 6.14. Isocontour for $Q = 60$ around the upper strut (left) and time derivative of surface pressure on the blade surface around the strut attachment (right) when they are located at $\theta = 90^\circ$ and 270°

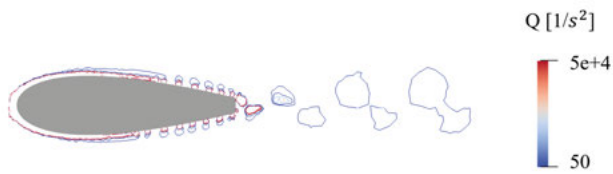


Figure 6.15. Contour plot for Q of the upper strut located at $\theta = 270^\circ$ at the plane sliced perpendicular to the span at 93% of rotor radius

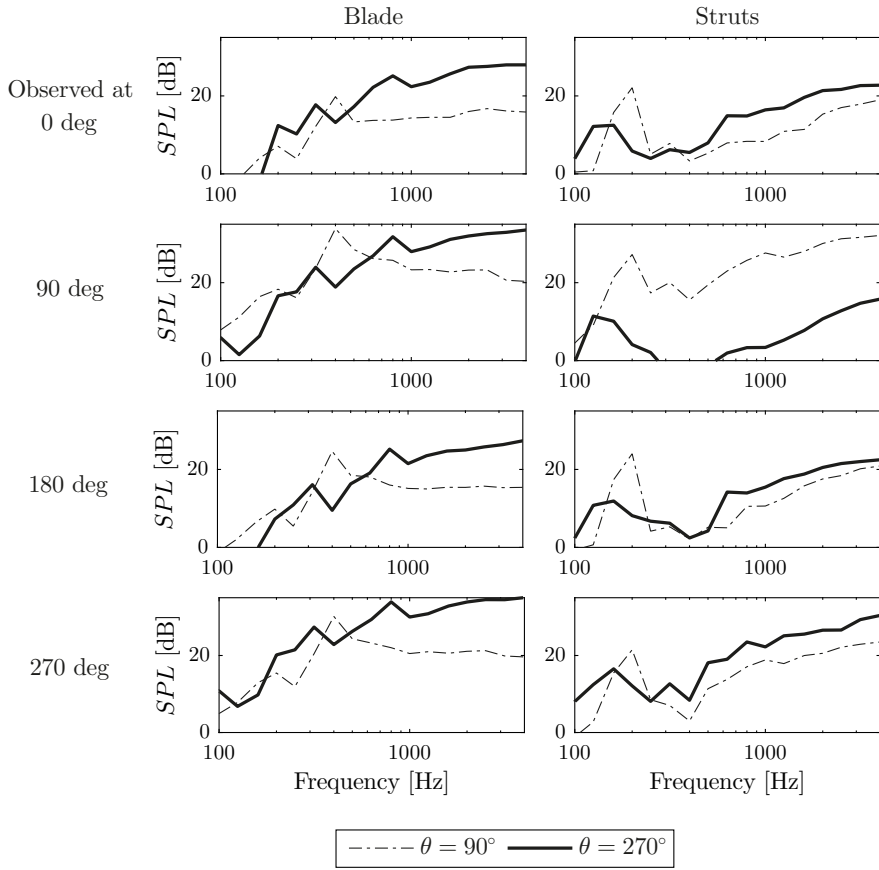


Figure 6.16. Spectra of the instantaneous SPL radiated from a single blade (left) and two struts (right) observed at 4 different azimuth angles (from top to bottom) when they pass at 90° (dotted) and 270° (solid line)

7. Conclusions

This thesis addresses the aerodynamics and aeroacoustics of VAWTs using computational fluid dynamics simulation. From this work, the following can be concluded:

- The prediction method for aerodynamic noise based on the LES and the acoustic analogy is validated for a static single airfoil case. The prediction is able to capture the dominant frequency, but fails to reproduce the broadband characteristics highly accurately.
- Simulations are performed to study the aerodynamic behavior of the 12 kW VAWT, and the results show the significant influence of struts on the blade forces. While there is no pronounced influence on the total normal force of the blade, the blade force is reduced at the attachment points of the struts, as well as over a large area of the blade section in the downwind side where the blade interacts with the wake created by blades and struts upstream.
- The performance of three different numerical models, namely, the CFD model, the ALM, and the vortex model, is compared to examine how accurately each model is able to reproduce the strut effect on the blade force. The CFD and vortex methods show prominent differences by including the struts in the models at middle and high tip speed ratios, while the ALM does not present such distinctive features. The CFD model is superior for predicting the strut effect at low tip speed where large dynamic stall is expected to occur.
- The aerodynamic noise of the VAWT operating at high tip speed ratio is simulated and the predicted noise is validated against measurement data. The sound is recorded at several azimuthal directions, and the measured spectra present the broadband noise centered at around 800 Hz. The spectra of the SPL observed at a radial distance of 1.4 rotor diameter is predicted with differences of a few decibels, but the discrepancies become more pronounced at double distance, probably because the effect of the ground reflection is neglected in the simulation.
- The simulation indicates that the loading noise dominates over the thickness noise for this VAWT operating at high tip speed ratio. The simulation shows the attached flow around the blade during revolution, as well as small vortices convected on both sides of the blade surface, which can be assumed to contribute to the trailing edge noise.

- The struts produce less noise than the blade, but they generate the tonal sound with moderate sound level at low frequency. The tonal noise is caused due to the vortices created in the separated boundary layer on the strut surface and at the blunt trailing edge.
- It can be considered that the main sound sources are generated from the blade rotating in the downwind side, as the simulation shows that the noise observed at several azimuth directions tends to be louder when the blade passes in the downwind than in the upwind half.

8. Future work

A number of recommendations for future research arise from this thesis:

- The influence of the struts on the blade force has been demonstrated here, but their impact on the rotor performance needs to be studied as well.
- A more precise comparison should be performed to better validate the noise prediction model. During measurements, the wind speed was unsteady, and thus the tip speed ratio was not constant. Recording over a longer time span will produce measurement data that is more valuable for the evaluation of certain operational conditions.
- The atmospheric turbulence in the freestream needs to be properly considered in the prediction. Several experimental and numerical studies have shown that the turbulence intensity considerably determines the noise level of wind turbine. These findings should be considered in relation to the VAWT studied in this thesis.
- The assumption that the discrepancies between the prediction and the measurement arise due to the effect of the ground reflection should be confirmed by further research. The reflected noise level can generally vary by more than 10 dB, depending on the impedance of the ground surface and the relative positions between the sound sources and the observer. Therefore, it might be crucial to consider the ground effect in prediction.
- The high tip speed ratio case is studied in the thesis, but the prediction should be validated for other operational conditions as well. Dynamic stall, which is expected to occur at low tip speed ratio, will create noise sources different from those at high tip speed ratio.
- Different configurations for blades and struts which can mitigate the noise should be proposed. It is expected that blades with a different airfoil profile, or a different shape of blade tip, generate a different total sound level. It could also be worthwhile to test if low noise emission is achieved by improving the geometry around the strut attachment points where the flow is significantly disturbed.

9. Summary of papers

This chapter presents a short summary of the papers included in this thesis.

Paper I

LES prediction for acoustic noise of airfoil at high angle of attack

The aerodynamic noise generated from a NACA 0012 airfoil under stall condition is simulated using LES and the acoustic analogy. Most of numerical works investigate noise for an airfoil at low angles of attack before a stall point, but few predictions have been performed for stall noise. This paper studies the airfoil at 15.6° angle of attack, where the flow around the airfoil is expected to be stalled. The predicted noise is compared with measurement data for validation. The wind tunnel configuration causes the downwash effect, thus RANS simulations reproducing the experimental conditions are conducted to determine the effective angle of attack. The noise from the airfoil under the condition studied here produces a tonal peak caused due to large-scaled vortices shed in the wake, and the results show that the prediction model is able to capture this dominant vortex shedding frequency in the spectrum.

Paper II

Numerical prediction of noise generated from airfoil in stall using LES and acoustic analogy

This paper studies the numerical method using LES and the Curle's acoustic analogy to predict noise radiated from a NACA 0012 airfoil at stall condition. It is especially challenging to predict the noise for a stalled airfoil, as the flow around the airfoil involves large-scaled vortex shedding, and this turbulence structure needs to be fully captured. Therefore, the spanwise correction is applied in this study to statistically estimate the total noise from the sound source of the limited span section in the simulation. The predicted spectrum of the sound pressure level is compared with measurement data, and it is shown that using the spanwise correction improves the prediction of tonal stall noise level.

Paper III

A numerical study of strut influence on blade forces of vertical axis wind turbine using computational fluid dynamics simulation

The influence of the struts on the aerodynamic forces of the VAWT blade is numerically investigated in this paper. It is known that horizontally attached struts decrease the rotor performance due to the drag produced, although this impact has not yet been sufficiently evaluated. In this study, three-dimensional RANS simulations are conducted to solve a flow field around the 12 kW H-rotor VAWT operating at high tip speed ratio. The blade force distribution is compared between two cases simulated with and without struts. The results show that the total normal force during revolution does not represent distinctive differences. However, the pronounced influence of the struts is observed in the blade force distribution. It is found that the force is reduced not only at the strut attachment points, but also over the large area of the blade section in the downwind side where the wake from the struts interact with the blades.

Paper IV

Comparison of three-dimensional numerical methods for modeling of strut effect on aerodynamic forces of a vertical axis wind turbine

This paper compares the performance of three different numerical models for predicting the blade force of the VAWT. The focus is to analyze how accurately each model is able to reproduce aerodynamic forces considering the strut effect. Flow fields around the H-rotor VAWT are simulated using the full CFD model, the actuator line model, and the vortex model for two cases with and without struts included. Three tip speed ratios are examined, and the results show that the CFD and vortex models clearly present the influence of the struts on the force distribution along the blade at middle and high tip speed ratios. The CFD model performs better than the other two models, especially at low tip speed ratio. This is because dynamic stall is expected to occur in this operational regime, and the CFD model is able to simulate the stall phenomenon accurately.

Paper V

Aeroacoustic noise prediction of a vertical axis wind turbine using Large Eddy Simulation

Aerodynamic noise prediction for the 12 kW VAWT is performed using LES and the acoustic analogy in this paper. Empirical models are commonly used to predict wind turbine noise, but few studies have investigated methods based

on CFD simulations which require higher computational cost but are more accurate. An incompressible flow is solved using LES to calculate the sound sources, and the sound propagation is estimated using the Ffowcs-Williams and Hawkings acoustic analogy. The noise generated from the turbine operating at high tip speed ratio is predicted, and the calculated sound pressure is compared with measurement data. The simulation is able to reproduce the sound level in the dominant frequency range with reasonable accuracy, but large discrepancies are found for the noise observed at a larger distance from the rotor. The results also indicate that the received sound tends to be larger when the blade passes in the downwind than in the upwind side.

10. Acknowledgements

I would like to express my gratitude to Prof. Hans Bernhoff, my main supervisor, for giving me a valuable opportunity to complete my PhD work. I also would like to thank Anders Goude, my supervisor, for all his great support and help. Thank you for dedicating a lot of your time for me and providing me important knowledge. I highly respect your attitude of patience and sincerity towards science, and learned many things as a great researcher.

I would also like to thank Prof. Mats Leijon for welcoming me as a member of the Division of Electricity and providing a lively environment.

Thank you Marcus Berg, Olle Svensson, and Karl Bolin for your kind support that was necessary to carry out the measurements in Marsta. My work couldn't have been done without your help.

I would like to thank all of my good colleagues at the Division. It was nice moment at work, and thanks a lot especially to those who are very open-minded and always included me to meeting up after work and at weekends. It really made my life in Sweden comfortable. It was great experience to work together with Victor in the same field, and you inspired me a lot in many aspects.

My gratitude goes to Ingrid Ringård, Linn Eriksson, Thomas Götschl, and all other administrative, financial and IT staff. Their help made my work run smoothly.

I would like to acknowledge the financial support from the Yoshida Scholarship Foundation that made my study possible. I would also like to thank the STandUP for Energy for funding my research activities.

Big thanks to Anke Johannmeyer for kindly offering language editing for this thesis.

I would like to thank to Claes-Göran Sjösten and Birgitta Sjösten, my landlords. They so kindly took care of me all the time during my stay in Uppsala. I was very happy to stay at your place and cannot express how much grateful I am as to my 'second' parents.

Last but not least, I want to note that my study couldn't be achieved without great support from my family. Regardless of long distance, my parents, brother and sister have always encouraged me under whatever circumstances.

11. Svensk sammanfattning

Denna avhandling undersöker aeroakustisk modellering av vertikalaxlade vindkraftverk genom att använda beräkningsströmningsmekanik (CFD). En låg ljudnivå från vindkraftverk är nödvändig, men det finns inte tillräcklig kunskap om källan till ljudet eller hur man kan reducera det, speciellt för vertikalaxlade vindkraftverk. I denna avhandling beräknas ljudnivån från CFD simuleringar och akustiska analogin för att ge bättre förståelse för mekanismerna som genererar ljud för vertikalaxlade vindkraftverk.

Som första steg valideras beräkningsmodellen för ljudemission för en ensam statisk vingprofil genom att LES (large eddy simulation) används för att beräkna ljudkällan. Ljudet beräknas för en NACA 0021 vingprofil som överstegrar med Reynolds tal 500 000 och Machtal 0.2. Endast en tiondel av vingens spännvidd modelleras och en spännviddskorrektion används för att beräkna totala ljudgenereringen. Den beräknade ljudtrycknivåns spektrum återskapar den dominerande toppens frekvens, vilken orsakas av de periodiska virvlarna som introduceras i flödet. Däremot så överskattas ljudnivån vid toppen och beräkningen har begränsad precision för bredbandskaraktistiken hos spektrumet.

Det aerodynamiska beteendet hos ett vertikalaxlat vindkraftverk undersöks via CFD med fokus på modellering av bärmarna som håller upp bladen. Det är nödvändigt att ta hänsyn till bärmarnas inverkan för att noggrant kunna bestämma krafterna på turbinbladen, och tre olika numeriska modeller jämförs för att avgöra hur exakt varje modell kan modellera bärmarnas påverkan. Normalkraften på bladen simuleras med en komplett CFD modell, med aktuatorlinjemodellen och med en virvelmodell för tre olika löptal. Alla tre modellerna ger liknande värden för den totala normalkraften under varvet när man jämför fallen om bärmarna inkluderas eller inte. Däremot ger kompletta CFD modellen och virvelmodellen en noterbar förändring i hur normalkraften fördelar sig längs bladets spännvidd när bärmarna inkluderas. Aktuatorlinjemodellen ger ingen sådan distinkt förändring p.g.a. bärmarna. Den kompletta CFD modellen ger bättre värden än de andra modellerna, speciellt vid låga löptal. Detta kan förklaras med att dynamisk överstegring sker vid låga löptal, och varken aktuatorlinjemodellen eller virvelmodellen inkluderar virvlarna som släpps från framkant på bladen. Utöver detta analyseras ett löptal mer i detalj med kompletta CFD modellen där bärmarna påverkar rotorns prestanda märkbart. Resultaten visar att kraften längs bladet reduceras, inte bara vid fästpunkten mellan bärmarm och blad, utan också över en stor del av bladet när det befinner sig på nedströms sida av turbinen, där vaken från bärmarna kan interagera med bladen. Den lägre kraften på bladen observeras

också rund fästpunkten för bärmarna mot bladen när bladen rör sig på uppströms sida av turbinen.

Slutligen beräknas ljudet som genereras från ett vertikalaxlat vindkraftverk som arbetar vid högt löptal med LES. Det akustiska spektrumet studeras på avstånden 1.4 och 2.8 rotordiametrar från turbinens centrum för flera azimuthala vinklar både experimentellt och via simuleringar. Jämförelser mellan simuleringar och mätningar visar att den dominerande toppen för ljudtrycksnivån runt 800 Hz återskapas med den numeriska modellen med en avvikelse på några decibel för det kortare avståndet. Skillnaderna mellan mätningar och simuleringar är större för det längre avståndet, vilket kan orsakas av att reflektionerna mot marken ignoreras i simuleringarna. Medan ljudet från bladens tjocklek dominerar för små vertikalaxlade vindkraftverk, erhålls här att ljudet i huvudsak genereras när bladen generera stor lyftkraft. Simuleringarna visar att flödet kring bladen i huvudsak är vidhäftat under varvet. Små virvlar som rör sig över en stor del av bladets yta observeras också, vilka kan antas bidra till ljudemissionen från blandens bakkant. Utöver detta tyder resultaten på att ljudet man hör är större från när bladen rör sig i nedströms halva av rotationen, än när de rör sig uppströms. Förklaringen till detta är antagligen bladen nedströms interagerar med vaken som skapats uppströms. Turbulensen från atmosfäriska gränsskiktet är inte inkluderat i simuleringarna, men skulle också kunna vara en stor källa till ljud för denna turbin. Turbulensens påverkan på totala ljudemissionen är något som behöver studeras ytterligare för att noggrant kunna förstå och beräkna ljudgenereringen.

12. 研究概要

本論文では、数値流体力学（CFD）解析を基にした垂直軸型風車の流体騒音の予測に関する手法について検証する。風力発電の市場が拡大する一方で風車の騒音低減がひとつの技術課題となっており、騒音を事前に予測することが設計、設置場所の選定などにおいて求められている。本研究においては騒音源に関連する風車周りの流れの特徴について考察し、音源となる流れ場と音の伝播を分離して計算する分離解法を用いた空力音の予測を行う。

始めに単体翼周りの騒音に関して、その空力音の予測精度について検証する。音源となる翼周りの流体流れはLES（Large Eddy Simulation）により求め、その結果を基にCurleの音響学的類推法により音場を算出する。ここではRe数が 5×10^5 、マッハ数が0.2の流れ中に置かれた失速状態のNACA 0012翼について検討する。参照する実験で用いられた翼モデルの全スパン長に対しその10%長さをLESにより解析するため、計測された全音圧を求めるためにスパン方向の乱流の相関を基にした音圧の補間法を適用する。この条件下においては翼周りに約500 Hzで後流渦が生じるが、音圧スペクトルを比較した結果、予測手法はこの主要な周波数を捉えることが出来た。しかし主要周波数を中心とした広帯域のスペクトル形状をより高精度に予測することが課題となった。

ストラットの存在により垂直軸型風車の効率が下がることが知られているが、次に垂直軸型風車の空力的挙動について特にストラットがブレードに与える影響に焦点を置き考察を行う。ブレード周りの流れを高精度に求めるには適切にストラットの影響を考慮する必要があるが、そこで12 kWの直線翼形垂直軸型風車に関してその影響を加味した3つの異なる数値モデルの予測精度の比較を行う。CFD手法、Actuator line手法、渦法を用い、ブレードに作用する半径方向の荷重を3通りの周速比の場合において解析した。どの手法においても一回転中のブレードの総荷重ではストラットを解析に含めた場合でもほとんど差異は見受けられなかった。しかしCFD手法と渦法においては、ブレードの高さごとの荷重分布でストラットの大きな影響が現れた。ブレード上の荷重分布はストラットとの接続部付近で減少するが、さらにストラットから生じる後流と干渉する広範囲にわたるブレードの表面部においても減少は見られた。Actuator line手法と渦法では動的失速の現象をモデルに含んでいないために、特に動的失速が起こる低周速比においてはCFD手法による予測が他の2手法より優れていることが示された。

最後に同垂直軸型風車に関して、LESとFfowcs Williams-Hawkings類推法を用い高周速比の場合の騒音の予測とその精度の検討を行った。予測精度の検証のために、回転中心から1.4と2.8ローター直径に当たる半径距離において複数の方位角から音圧の計測を行った。計測した音圧レベルのスペクトルはどの計測箇所においても約800 Hzを中心とした広帯域のピークを示したが、1.4ローター直径の距離の場合、主要な周波数の範囲において数デシベルの誤差内で音圧が推定された。しかし距離が2倍となった場合は音圧は過少に予測され、誤差がより大きくなった。計測においては音が音源から観測点まで伝播する際に地表面の影響を受けることが予想されるが、解析ではその影響を無視していることが誤差の一つの要因として考えられる。小型の垂直軸型風車を扱っているこれまでの研究では翼厚音（thickness noise）が主要な音源であると明らかにしているが、この風車ではより大型で回転数が低いため荷重音（loading noise）が主な騒音源とわかった。また計測時において風車はブレードの回転周期に伴ってはっきりとした空気を切る音を発していたが、解析結果よりこれはブレードが回転の下流側を通過する時に生じると推察された。これは、下流側を通過するブレードが上流側で生じる後流と干渉しブレードの表面圧力がより変動することがその騒音の発生に寄与していると考えられる。解析では主流中の乱れは考慮していないが、実際の風車の音圧レベルは流入乱れ騒音に大きく左右されている可能性がある。この影響を考慮することで予測の精度が改善されるか検証することが、この風車の主要な音源をより明らかにする上でも今後の課題となった。

References

- [1] WWEA. World wind capacity at 650,8 GW, corona crisis will slow down markets in 2020, renewables to be core of economic stimulus programmes. <https://library.wwindea.org>, 2020 (accessed: 2020-06-04).
- [2] WindEurope. Wind energy in Europe in 2019 - Key trends and statistics. <https://windeurope.org/about-wind/statistics>, 2020 (accessed: 2020-06-04).
- [3] Wind Energy The Facts. Growth of wind turbine size. <https://www.wind-energy-the-facts.org>, 2019 (accessed: 2020-06-04).
- [4] F. Blaabjerg and K. Ma. Future on power electronics for wind turbine systems. *IEEE Journal of emerging and selected topics in power electronics*, 1(3):139–152, 2013.
- [5] Y. Kumar, J. Ringenberg, S. S. Depuru, V. K. Devabhaktuni, J. W. Lee, E. Nikolaidis, B. Andersen, and A. Afjeh. Wind energy: Trends and enabling technologies. *Renewable and Sustainable Energy Reviews*, 53:209–224, 2016.
- [6] Office of Energy Efficiency & Renewable Energy. Top Trends in Offshore Wind. <https://www.energy.gov>, 2019 (accessed: 2020-06-04).
- [7] The CDR. Darrieus vertical axis wind turbine. <http://canadiandesignresource.ca/miscellaneous/darrieus-vertical-axis-wind-turbine>, 2013 (accessed: 2020-06-06).
- [8] Ablison Energy. Types of Wind Turbines: Explained & Compared. <https://www.ablison.com/types-of-wind-turbines>, 2019 (accessed: 2020-06-06).
- [9] M. M. A. Bhutta, N. Hayat, A. U. Farooq, Z. Ali, S. R. Jamil, and Z. Hussain. Vertical axis wind turbine—A review of various configurations and design techniques. *Renewable and Sustainable Energy Reviews*, 16(4):1926–1939, 2012.
- [10] M. Islam, D. S. K. Ting, and A. Fartaj. Aerodynamic models for Darrieus-type straight-bladed vertical axis wind turbines. *Renewable and sustainable energy reviews*, 12(4):1087–1109, 2008.
- [11] W. Tjiu, T. Marnoto, S. Mat, M. H. Ruslan, and K. Sopian. Darrieus vertical axis wind turbine for power generation I: Assessment of Darrieus VAWT configurations. *Renewable Energy*, 75:50–67, 2015.
- [12] M. H. Mohamed, G. Janiga, E. Pap, and D. Thévenin. Optimal blade shape of a modified savonius turbine using an obstacle shielding the returning blade. *Energy Conversion and Management*, 52(1):236–242, 2011.
- [13] F. Toja-Silva, A. Colmenar-Santos, and M. Castro-Gil. Urban wind energy exploitation systems: Behaviour under multidirectional flow conditions—Opportunities and challenges. *Renewable and Sustainable Energy Reviews*, 24:364–378, 2013.

- [14] S. Eriksson, H. Bernhoff, and M. Leijon. Evaluation of different turbine concepts for wind power. *Renewable and Sustainable Energy Reviews*, 12(5):1419–1434, 2008.
- [15] D. Shepherd, D. McBride, D. Welch, K. N. Dirks, and E. M. Hill. Evaluating the impact of wind turbine noise on health-related quality of life. *Noise and Health*, 13(54):333–339, 2011.
- [16] O. Jianu, M. A. Rosen, and G. Naterer. Noise pollution prevention in wind turbines: status and recent advances. *Sustainability*, 4(6):1104–1117, 2012.
- [17] S. Wagner, R. Bareiss, and G. Guidati. *Wind turbine noise*. Environmental engineering. Springer Berlin Heidelberg, 1996.
- [18] T. F. Brooks, D. S. Pope, and M. A. Marcolini. Airfoil self-noise and prediction. *NASA Reference Publication No. 1218*, 1989.
- [19] C. K. W. Tam. Discrete tones of isolated airfoils. *The Journal of the Acoustical Society of America*, 55(6):1173–1177, 1974.
- [20] S. E. Wright. The acoustic spectrum of axial flow machines. *Journal of Sound and Vibration*, 45(2):165–223, 1976.
- [21] M. R. Fink. Fine structure of airfoil tone frequency. *The Journal of the Acoustical Society of America*, 63(S1):S22–S22, 1978.
- [22] R. W. Paterson, R. K. Amiet, and C. L. Munch. Isolated airfoil-tip vortex interaction noise. *Journal of Aircraft*, 12(1):34–40, 1975.
- [23] P. Moriarty and P. Migliore. Semi-empirical aeroacoustic noise prediction code for wind turbines. Technical report, National Renewable Energy Laboratory, Golden, Colorado, 2003.
- [24] P. Migliore, J. Van Dam, and A. Huskey. Acoustic tests of small wind turbines. In *42nd AIAA Aerospace Sciences Meeting and Exhibit*, 2004.
- [25] T. Rogers and S. Omer. The effect of turbulence on noise emissions from a micro-scale horizontal axis wind turbine. *Renewable Energy*, 41:180–184, 2012.
- [26] S. Buck, S. Oerlemans, and S. Palo. Experimental characterization of turbulent inflow noise on a full-scale wind turbine. *Journal of Sound and Vibration*, 385:219–238, 2016.
- [27] S. Oerlemans, P. Sijtsma, and B. M. López. Location and quantification of noise sources on a wind turbine. *Journal of sound and vibration*, 299(4-5):869–883, 2007.
- [28] S. Oerlemans, M. Fisher, T. Maeder, and K. Kögler. Reduction of wind turbine noise using optimized airfoils and trailing-edge serrations. *AIAA journal*, 47(6):1470–1481, 2009.
- [29] E. Möllerström, F. Ottermo, J. Hylander, and H. Bernhoff. Noise emission of a 200 kW vertical axis wind turbine. *Energies*, 9(1):19, 2016.
- [30] F. Ottermo, E. Möllerström, A. Nordborg, J. Hylander, and H. Bernhoff. Location of aerodynamic noise sources from a 200 kW vertical-axis wind turbine. *Journal of Sound and Vibration*, 400:154–166, 2017.
- [31] C. Pearson. *Vertical axis wind turbine acoustics*. PhD thesis, University of Cambridge, 2014.
- [32] F. W. Grosveld. Prediction of broadband noise from horizontal axis wind turbines. *Journal of propulsion and power*, 1(4):292–299, 1985.
- [33] M. V. Lowson. Assessment and prediction of wind turbine noise. Technical

- report, Flow Solutions Ltd., 1993.
- [34] W. J. Zhu, N. Heilskov, W. Z. Shen, and J. N. Sørensen. Modeling of aerodynamically generated noise from wind turbines. *Journal of Solar Energy Engineering*, 127(4):517–528, 2005.
 - [35] G. Leloudas, W. J. Zhu, J. N. Sørensen, W. Z. Shen, and S. Hjort. Prediction and reduction of noise from a 2.3 MW wind turbine. In *Journal of physics: conference series*, volume 75, 2007.
 - [36] A. Tadamasa and M. Zangeneh. Numerical prediction of wind turbine noise. *Renewable Energy*, 36(7):1902–1912, 2011.
 - [37] M. Ghasemian and A. Nejat. Aerodynamic noise prediction of a horizontal axis wind turbine using improved delayed detached eddy simulation and acoustic analogy. *Energy Conversion and Management*, 99:210–220, 2015.
 - [38] M. Maizi, M. H. Mohamed, R. Dizene, and M. C. Mihoubi. Noise reduction of a horizontal wind turbine using different blade shapes. *Renewable energy*, 117:242–256, 2018.
 - [39] M. H. Mohamed. Aero-acoustics noise evaluation of H-rotor Darrieus wind turbines. *Energy*, 65:596–604, 2014.
 - [40] M. Ghasemian and A. Nejat. Aero-acoustics prediction of a vertical axis wind turbine using Large Eddy Simulation and acoustic analogy. *Energy*, 88:711–717, 2015.
 - [41] J. Weber, S. Becker, C. Scheit, J. Grabinger, and M. Kaltenbacher. Aeroacoustics of Darrieus wind turbine. *International Journal of Aeroacoustics*, 14(5-6):883–902, 2015.
 - [42] M. J. Lighthill. On sound generated aerodynamically I. General theory. *Proceedings of the Royal Society of London. Series A. Mathematical and Physical Sciences*, 211(1107):564–587, 1952.
 - [43] N. Curle. The influence of solid boundaries upon aerodynamic sound. *Proceedings of the Royal Society of London. Series A. Mathematical and Physical Sciences*, 231(1187):505–514, 1955.
 - [44] J. Larsson, L. Davidson, M. Olsson, and L. E. Eriksson. Aeroacoustic investigation of an open cavity at low mach number. *AIAA journal*, 42(12):2462–2473, 2004.
 - [45] K. S. Brentner and F. Farassat. Modeling aerodynamically generated sound of helicopter rotors. *Progress in Aerospace Sciences*, 39(2-3):83–120, 2003.
 - [46] J. C. Lerner and U. Boldes. *Applied Aerodynamics*. BoD–Books on Demand, 2012.
 - [47] S. Glegg and W. Devenport. *Aeroacoustics of low Mach number flows: fundamentals, analysis, and measurement*. Academic Press, 2017.
 - [48] F. Farassat. Derivation of formulations 1 and 1A of farassat. *Technical Report NASA/TM-214853*, 2007.
 - [49] M. J. Crocker. *Handbook of noise and vibration control*. John Wiley & Sons, 2007.
 - [50] J. C. Hardin and D. S. Pope. An acoustic/viscous splitting technique for computational aeroacoustics. *Theoretical and computational fluid dynamics*, 6(5-6):323–340, 1994.
 - [51] J. Christophe, J. Anthoine, and S. Moreau. Trailing edge noise of a controlled-diffusion airfoil at moderate and high angle of attack. In *15th*

- AIAA/CEAS Aeroacoustics Conference (30th AIAA Aeroacoustics Conference)*, 2009.
- [52] J. H. Seo and Y. J. Moon. Aerodynamic noise prediction for long-span bodies. *Journal of Sound and Vibration*, 306(3-5):564–579, 2007.
 - [53] C. Kato, A. Iida, Y. Takano, H. Fujita, and M. Ikegawa. Numerical prediction of aerodynamic noise radiated from low mach number turbulent wake. In *31st Aerospace Sciences Meeting*, 1993.
 - [54] F. Pérot, X. Gloerfelt, C. Bailly, J. M. Auger, and H. Giardi. Numerical prediction of the noise radiated by a cylinder. In *9th AIAA/CEAS Aeroacoustics Conference and Exhibit*, 2003.
 - [55] M. Wang and P. Moin. Computation of trailing-edge flow and noise using large-eddy simulation. *AIAA journal*, 38(12):2201–2209, 2000.
 - [56] M. C. Jacob, J. Boudet, D. Casalino, and M. Michard. A rod-airfoil experiment as a benchmark for broadband noise modeling. *Theoretical and Computational Fluid Dynamics*, 19(3):171–196, 2005.
 - [57] M. O. L. Hansen. *Aerodynamics of wind turbines*. Routledge, 2015.
 - [58] S. Eriksson. *Direct driven generators for vertical axis wind turbines*. PhD thesis, Uppsala University, 2008.
 - [59] J. Kjellin. *Vertical axis wind turbines: Electrical system and experimental results*. PhD thesis, Uppsala University, 2012.
 - [60] F. Bülow. *A generator perspective on vertical axis wind turbines*. PhD thesis, Uppsala University, 2013.
 - [61] M. Rossander. *Electromechanics of vertical axis wind turbines*. PhD thesis, Uppsala University, 2017.
 - [62] P. Deglaire. *Analytical aerodynamic simulation tools for vertical axis wind turbines*. PhD thesis, Uppsala University, 2010.
 - [63] A. Goude. *Fluid mechanics of vertical axis turbines: Simulations and model development*. PhD thesis, Uppsala University, 2012.
 - [64] E. Dyachuk. *Aerodynamics of vertical axis wind turbines: Development of simulation tools and experiments*. PhD thesis, Uppsala University, 2015.
 - [65] V. Mendoza. *Aerodynamic studies of vertical axis wind turbines using the actuator line model*. PhD thesis, Uppsala University, 2018.
 - [66] S. Moreau, M. Henner, G. Iaccarino, M. Wang, and M. Roger. Analysis of flow conditions in freejet experiments for studying airfoil self-noise. *AIAA journal*, 41(10):1895–1905, 2003.
 - [67] T. F. Brooks, M. A. Marcolini, and D. S. Pope. Airfoil trailing-edge flow measurements. *AIAA journal*, 24(8):1245–1251, 1986.
 - [68] H. G. Weller, G. Tabor, H. Jasak, and C. Fureby. A tensorial approach to computational continuum mechanics using object-oriented techniques. *Computers in physics*, 12(6):620–631, 1998.
 - [69] A. Yoshizawa. Statistical theory for compressible turbulent shear flows, with the application to subgrid modeling. *The Physics of fluids*, 29(7):2152–2164, 1986.
 - [70] B. A. Singer, K. S. Brentner, D. P. Lockard, and G. M. Lilley. Simulation of acoustic scattering from a trailing edge. *Journal of Sound and Vibration*, 230(3):541–560, 2000.
 - [71] R. E. Sheldahl and P. C. Klimas. Aerodynamic characteristics of seven symmetrical airfoil sections through 180-degree angle of attack for use in

- aerodynamic analysis of vertical axis wind turbines. Technical report, Sandia National Labs., Albuquerque, NM (USA), 1981.
- [72] M. Drela. XFOIL: An analysis and design system for low Reynolds number airfoils. In *Low Reynolds number aerodynamics*, pages 1–12. Springer Berlin Heidelberg, 1989.
 - [73] F. R. Menter, M. Kuntz, and R. Langtry. Ten years of industrial experience with the SST turbulence model. *Turbulence, heat and mass transfer*, 4(1):625–632, 2003.
 - [74] A. Rezaeiha, H. Montazeri, and B. Blocken. On the accuracy of turbulence models for CFD simulations of vertical axis wind turbines. *Energy*, 180:838–857, 2019.
 - [75] F. Balduzzi, A. Bianchini, R. Maleci, G. Ferrara, and L. Ferrari. Critical issues in the CFD simulation of Darrieus wind turbines. *Renewable Energy*, 85:419–435, 2016.
 - [76] R. K. Angell, P. J. Musgrove, and R. A. M. Galbraith. The collected data for tests on a NACA 0021 aerofoil. Technical report, Department of Aeronautics & Fluid Mechanics, University of Glasgow, 1988.
 - [77] C. S. Ferreira, H. A. Madsen, M. Barone, B. Roscher, P. Deglaire, and I. Arduin. Comparison of aerodynamic models for vertical axis wind turbines. In *Journal of Physics: Conference Series*, volume 524. IOP Publishing, 2014.
 - [78] H. A. Madsen. *Actuator cylinder. A flow model for vertical axis wind turbines*. Institute of Industrial Constructions and Energy Technology, Aalborg University Centre, 1982.
 - [79] H. A. Madsen. *On the ideal and real energy conversion in a straight bladed vertical axis wind turbine*. Institute of Industrial Constructions and Energy Technology, Aalborg University Centre, 1983.
 - [80] J. Murray and M. Barone. The development of CACTUS, a wind and marine turbine performance simulation code. In *49th AIAA Aerospace Sciences Meeting including the New Horizons Forum and Aerospace Exposition*, 2011.
 - [81] E. Dyachuk, M. Rossander, A. Goude, and H. Bernhoff. Measurements of the aerodynamic normal forces on a 12-kW straight-bladed vertical axis wind turbine. *Energies*, 8(8):8482–8496, 2015.
 - [82] M. Rossander, E. Dyachuk, S. Apelfröjd, K. Trolin, A. Goude, H. Bernhoff, and S. Eriksson. Evaluation of a blade force measurement system for a vertical axis wind turbine using load cells. *Energies*, 8(6):5973–5996, 2015.
 - [83] F. Nicoud and F. Ducros. Subgrid-scale stress modelling based on the square of the velocity gradient tensor. *Flow, Turbulence and Combustion*, 62(3):183–200, 1999.
 - [84] J. F. Ainslie and J. Scott. Theoretical modelling of noise generated by wind turbines. *Wind Engineering*, 14(1):9–14, 1990.
 - [85] O. Marsden, C. Bogey, and C. Bailly. Direct noise computation of the turbulent flow around a zero-incidence airfoil. *AIAA journal*, 46(4):874–883, 2008.
 - [86] E. Manoha, C. Herrero, S. Ben Khelil, P. Guillen, P. Sagaut, and I. Mary. Numerical prediction of airfoil aerodynamic noise. In *8th AIAA/CEAS Aeroacoustics Conference & Exhibit*, 2002.
 - [87] F. Farassat. Linear acoustic formulas for calculation of rotating blade noise. *AIAA journal*, 19(9):1122–1130, 1981.

- [88] W. R. Wolf, J. L. F. Azevedo, and S. K. Lele. Convective effects and the role of quadrupole sources for aerofoil aeroacoustics. *Journal of Fluid Mechanics*, 708:502–538, 2012.
- [89] J. Kjellin, F. Bülow, S. Eriksson, P. Deglaire, M. Leijon, and H. Bernhoff. Power coefficient measurement on a 12 kW straight bladed vertical axis wind turbine. *Renewable energy*, 36(11):3050–3053, 2011.
- [90] J. Kjellin and H. Bernhoff. Electrical starter system for an H-rotor type VAWT with PM-generator and auxiliary winding. *Wind Engineering*, 35(1):85–92, 2011.
- [91] S. Eriksson, A. Solum, M. Leijon, and H. Bernhoff. Simulations and experiments on a 12 kW direct driven PM synchronous generator for wind power. *Renewable Energy*, 33(4):674–681, 2008.
- [92] A. Goude and M. Rossander. Force measurements on a VAWT blade in parked conditions. *Energies*, 10(12):1954, 2017.
- [93] J. Yen and N. A. Ahmed. Enhancing vertical axis wind turbine by dynamic stall control using synthetic jets. *Journal of Wind Engineering and Industrial Aerodynamics*, 114:12–17, 2013.

Acta Universitatis Upsaliensis

*Digital Comprehensive Summaries of Uppsala Dissertations
from the Faculty of Science and Technology 1996*

Editor: The Dean of the Faculty of Science and Technology

A doctoral dissertation from the Faculty of Science and Technology, Uppsala University, is usually a summary of a number of papers. A few copies of the complete dissertation are kept at major Swedish research libraries, while the summary alone is distributed internationally through the series Digital Comprehensive Summaries of Uppsala Dissertations from the Faculty of Science and Technology. (Prior to January, 2005, the series was published under the title "Comprehensive Summaries of Uppsala Dissertations from the Faculty of Science and Technology".)

Distribution: publications.uu.se
urn:nbn:se:uu:diva-426038



ACTA
UNIVERSITATIS
UPSALIENSIS
UPPSALA
2021